Development of a High Refractive Index Aerogel Cherenkov Counter for the Spectroscopy of η' Mesic Nuclei

Master Thesis

by

Yoshiki Tanaka

January 2013

Department of Physics, Graduate School of Science,

The University of Tokyo

Abstract

In this thesis, development of a high-refractive-index aerogel Cherenkov counter and a test experiment of this counter is described.

We have developed a high-refractive-index aerogel Cherenkov counter (HIRAC) for the particle identification in the spectroscopy of η'-nucleus bound states (η' mesic nuclei) with the (p,d) reaction. In this experiment, a 2.5 GeV proton beam will be injected to a carbon target, and the momenta of ejectile deuterons will be measured at a downstream focal plane of a spectrometer. However, in addition to the signal deuterons ($\beta \sim 0.83$), a large number of background protons ($\beta \sim 0.95$) are expected to reach the focal plane. The purpose of HIRAC is to reject these background protons at the trigger level.

To distinguish the two velocities, a silica aerogel with a refractive index of $n = 1.18$ was adopted as a Cherenkov radiator. We designed this detector and optimized the internal structure by simulation so that its performance was maximized.

We performed a test experiment of HIRAC. With a deuteron beam of $T = 1900$ MeV/u ($\beta = 0.944$), a sufficient number of photoelectrons were observed. The background rejection capability expected in the main experiment was evaluated to be higher than 99.9 % in average with a nine-photoelectron threshold. Also, with this threshold, 99.5 % rejection capability is expected at the least-sensitive incident position of HIRAC. This rejection capability is quite sufficient for the main experiment.

Signal overkill was also evaluated using a deuteron beam of $T = 800$ MeV/u ($\beta = 0.843$). As a result, the signal overkill probability was deduced to be 2 % - 4 % at the nine-photoelectron threshold, depending on the incident beam position. Such position dependence of the signal overkill may distort the final spectrum. Therefore, in the main experiment, improvements to reduce the overkill or reduce its position dependence are needed.

Contents

List of Figures

List of Tables

Chapter 1

Introduction

1.1 Physics Motivation

One of the important topics in the present hadron physics is to understand hadron properties in nuclear matter. In vacuum, chiral symmetry of QCD is spontaneously broken, and chiral condensate, which is the order parameter of chiral symmetry, has a finite value of $\langle \bar{q}q \rangle = -(250\,\mathrm{MeV})^3$ [1, 2]. In finite density or temperature, this symmetry is known to be partially restored, and $|\langle \bar{q}q \rangle|$ is considered to be decreased by about 30% already at the normal nuclear density [3, 4, 5]. From hadron properties in nuclear density, effects of the chiral symmetry breaking can be studied.

The η' meson is one of the pseudoscalar mesons, which has a peculiarly large mass (958 MeV/c^2), compared to the other pseudoscalar mesons, π, K, and η. This heavy mass is theoretically understood as an effect of quantum $U_A(1)$ anomaly, and the strength of this effect is considered to be related to the chiral condensate [6, 7]. Then, in nuclear medium, due to the partial restoration of chiral symmetry, the mass of η' may be reduced. For instance, the NJL model calculation shows a mass reduction of 150 MeV at normal nuclear density [8, 9]. Since such mass reduction serves as an attractive potential between an η' and a nucleus, η' meson-nucleus bound states may exist [9, 10]. An experimental study on such η' mesic states may provide understanding of above theoretical scenario about mass generation of the η' meson and its relation to the chiral condensate.

So far, there is no direct experimental information on the η' mass in medium, but the η'-nucleon scattering length, which is related to the mass reduction. In Moskal *et al.* [11], from measurements of $pp \to pp\eta'$ reaction near threshold, scattering length of η'-nucleon interaction was evaluated to be of the order of 0.1 fm. This suggests that interaction between the η' meson and nucleon is not strong, and it seems difficult to understand the small scattering length and the scenario of large mass reduction at the same time [10]. Therefore, an experiment on η' mesic nucleus states will give understanding for this situation.

Recently, as for the in-medium width, the CBELSA/TAPS collaboration deduced a small absorption width of η' at normal nuclear density [12]. They measured mass-number dependence of the transparency ratio and concluded the η' absorption width of 15-25 MeV at normal nuclear density for the average η' momentum of 1050 MeV/c. This suggests that the decay width of η' meson-nucleus bound states could be small as well. Therefore, η'-nucleus bound states may be observed as distinct peaks experimentally.

Motivated by these backgrounds, we are planning a spectroscopy experiment of η' mesic nuclei. In the next section, the plan of the experiment is described.

1.2 Plan of the Spectroscopy of η' Mesic Nuclei at GSI

1.2.1 Experimental Principle

We are planning to perform a missing mass spectroscopy of the ^{12}C(p,d) reaction near the η' emission threshold at GSI in Darmstadt, Germany [13, 14]. In this experiment, a 2.5 GeV proton beam accelerated by the Heavy Ion Synchrotron (SIS) will be injected to a ^{12}C target. Then, the ^{12}C(p,d) reaction will occur, as illustrated in Figure 1.1, and the momenta of the ejectile deuterons will be analyzed to obtain missing masses of the reaction.

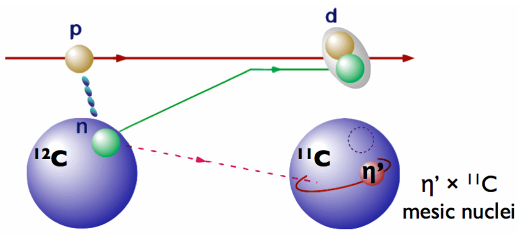

FIGURE 1.1: A schematic view of the ^{12}C(p,d) reaction producing an η' mesic nucleus.

One feature of this experiment is an inclusive measurement, in which only the ejectile deuterons are measured. This leads to a simple analysis, as no assumption on decay processes of η' mesic states is necessary. However, the signal-to-noise ratio in the spectrum becomes poor, because of quasi-free meson (not η') production processes dominated by multi-pion production ($p+N \to d+\pi$'s). This can be overcome by a high-statistics measurement using the intense primary beam available at SIS in GSI and a thick production target.

1.2.2 Experimental Method

We will use the Fragment Separator (FRS) as a spectrometer in order to measure the momenta of the ejectile deuterons. Figure 1.2 shows the setup at FRS. We will adopt a momentum-dispersive optics from the target to the final focal plane S4, and install two sets of multi-wire drift chambers (MWDCs) at this S4 area as tracking detectors. Then, by measuring positions of the deuterons, their momenta and thereby missing masses in the reaction will be obtained. Owing to good resolution of FRS, the overall spectral resolution is estimated to be about 1.6 MeV, which is sufficiently small compared to the expected decay width.

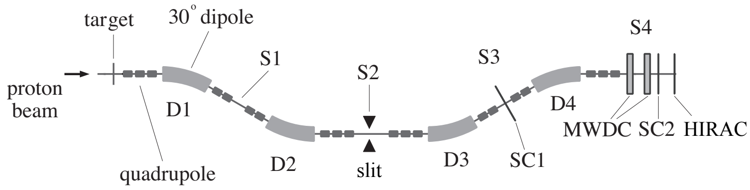

Figure 1.2: A schematic view of the setup of the main experiment at FRS.

In the experiment, particle identification is necessary, because not only the signal deuterons, but also many protons produced by the (p,p') reaction in the target are expected to reach the final focal plane. These background protons have a velocity of $\beta \sim 0.95$ and an expected rate of about 50 kHz, while the signal deuterons have a velocity of $\beta \sim 0.83$ and an expected rate of about 0.5 kHz. In order to reject these protons, we will install a high-refractive-index aerogel Cherenkov counter (HIRAC) at S4 and scintillation counters (SC1, SC2) at S3 and S4, as shown in Figure 1.2. At the trigger level, HIRAC will be used in veto mode to reduce the proton rate to the order of 0.1 kHz. Then, in the off-line analysis, by use of time-of-flight between S3 and S4, we expect almost all these background protons can be rejected.

We also expect secondary background produced by the intense primary beam dumped in the first dipole magnet, denoted by D1 in Figure 1.2. This background can be suppressed by adopting an appropriate optics mode. We will adopt a momentum-compaction optics to the middle focal plane S2. With this optics mode, all particles originating from the target will be focused at one point regardless their momenta. Therefore, by installing slits at this middle focal plane, the secondary background can be suppressed.

1.2.3 Simulated Inclusive Spectra

We have simulated inclusive spectra of the ^{12}C(p,d) reaction to discuss the experimental feasibility of finding peak structures of η' mesic states. First, the cross section of background processes in the inclusive (p,d) spectrum, which is mainly dominated by the multi-pion production, was estimated based on the COSY/ANKE data and simulation [15]. Then, combining with the formation cross sections of η' mesic states calculated by Nagahiro *et al.* [16], we simulated inclusive spectra expected in 4.5-day data acquisition.

Figure 1.3 shows the simulation results for several cases of different in-medium mass reductions and widths. When the mass reduction is large and the width is small, distinct peak structures can be observed. However, with smaller mass reduction and broader width, signal-to-noise ratio becomes much worse, and therefore peak structures can not seen in this case. When $|V_0| = 150$ MeV, as predicted by the NJL model calculations [8, 9], and $|W_0|$ is less than 12.5 MeV, as reported by the CBELSA/TAPS experiment [12], there is a large chance to observe peaks in the spectrum experimentally.

1.3 Requirements for the Aerogel Cherenkov Detector

The purpose of the HIRAC detector is to reject the background protons at the trigger level, as described in 1.2.2. In this section, requirements for HIRAC are summarized.

Figure 1.4 shows the momentum range of interest and corresponding velocity. Since the velocity range is 0.82 - 0.85 for the deuterons and 0.94 - 0.96 for the protons, a refractive index of Cherenkov radiator between 1.06 and 1.18 is necessary.

Conditions of the signal deuterons and the background protons at the HIRAC position are tabulated in Table 1.1. The expected rate is about 0.5 kHz for the deuterons and 50 kHz for the protons, and the expected beam size is $(x, y) \sim (\pm 120\text{mm}, \pm 30\text{mm})$ with the angular spread of $(x', y') \sim (\pm 19\text{mrad}, \pm 13\text{mrad})$, where x is the horizontal axis normal to the beam direction, and y is the vertical axis. To reduce the background rate to the order of 0.1 kHz, about 99.5 % rejection capability for this beam spread is required.

TABLE 1.1: Signal and background conditions at HIRAC.

	signal deuteron	background proton
velocity ($\beta = v/c$)	0.82 - 0.85	0.94 - 0.96
expected rate	0.5 kHz	50 kHz
spatial spread (x, y)	(±120 mm, ±30 mm)	(±120 mm, ±30 mm)
angular spread (x', y')	(±19 mrad, ±13 mrad)	(±19 mrad, ±13 mrad)

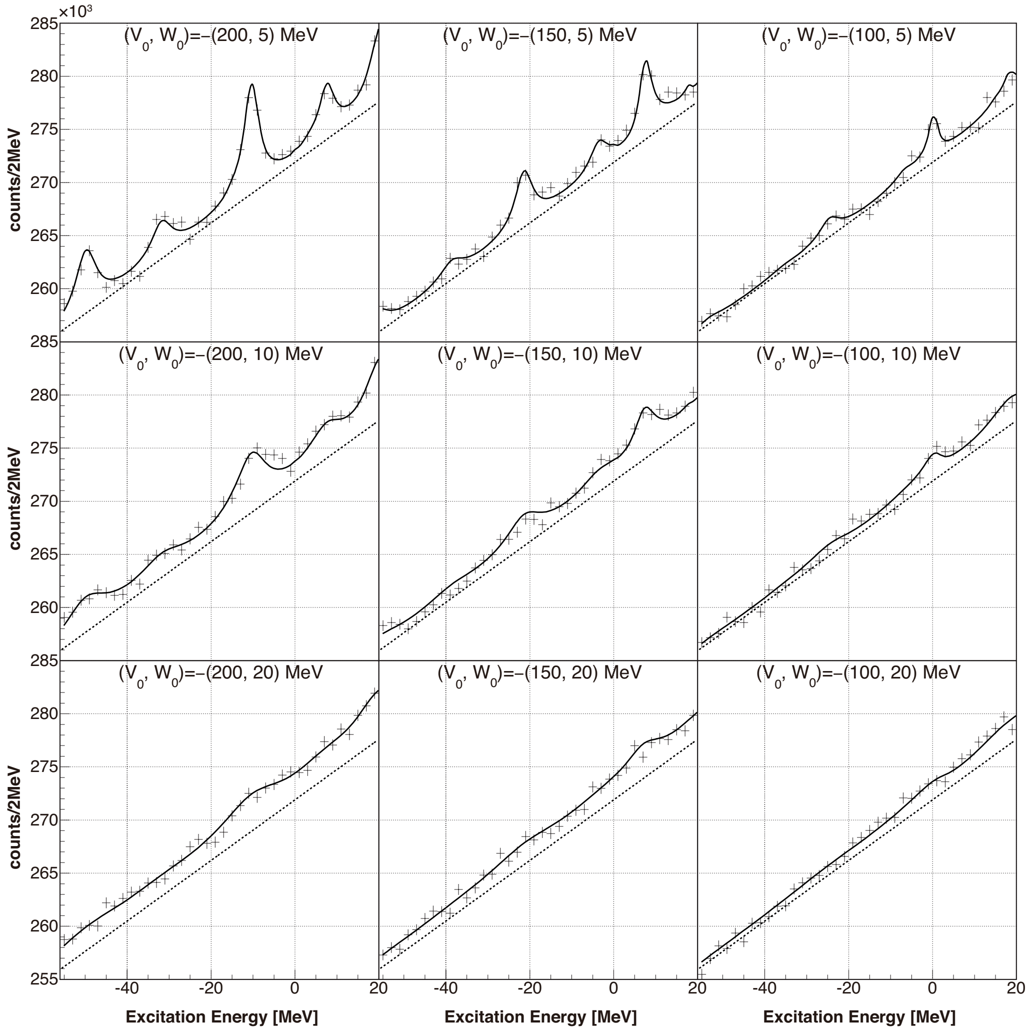

FIGURE 1.3: Simulated inclusive spectra expected in 4.5-day data acquisition. V_0 is the real part and W_0 is the imaginary part of the optical potential at normal nuclear density. In-medium mass reduction and width correspond to $|V_0|$ and $2|W_0|$, respectively. The amount of the background processes is shown by the dashed line.

1.4 Thesis Outline

In this thesis, development and a text experiment of the HIRAC detector for the spectroscopy of η' mesic nuclei is described. The design and simulated performance of HIRAC are described in chapter 2. Next, in chapter 3, the test experiment of HIRAC performed at GSI in November 2012 is explained, and its analysis and results follow in chapter 4. In chapter 5, we discuss expected performance and possible improvements in the main experiment, and we conclude this thesis in chapter 6.

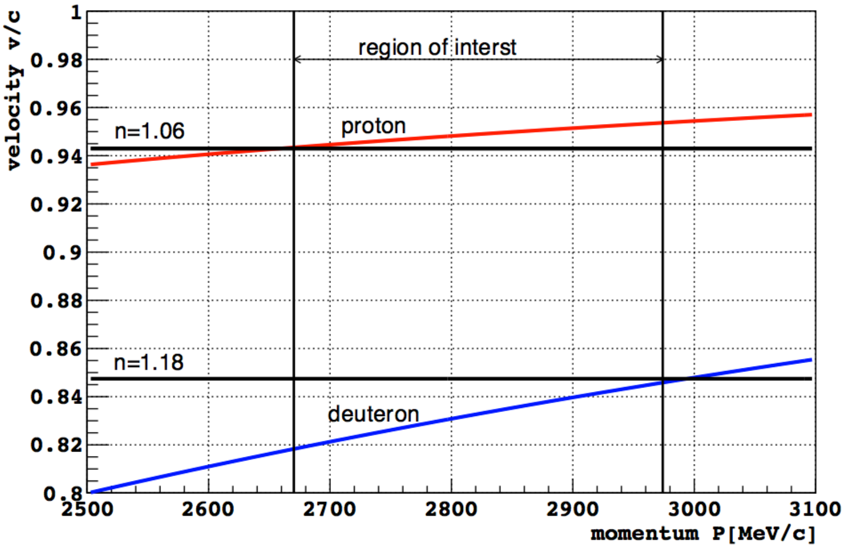

FIGURE 1.4: Velocity of the background protons (red) and signal deuterons (blue) in the momentum region of interest is shown. The black lines show the Cherenkov threshold velocity for refractive indices of 1.06 and 1.18.

Chapter 2

Development of HIRAC

2.1 Overview of Cherenkov Detectors

Cherenkov detectors are devices detecting Cherenkov photons. When charged particles move in a material faster than the speed of light in that material, Cherenkov photons are emitted to the angle θ from the direction of the movement given by the following formula:

$$\cos\theta = \frac{1}{n\beta}, \tag{2.1}$$

where n is the refractive index of the material, and β is the speed of the particle divided by the speed of light in vacuum. The number N of the Cherenkov photons radiated per length z per wavelength λ is expressed as

$$\frac{d^2N}{dzd\lambda} = \frac{2\pi\alpha Z^2}{\lambda^2}\left(1 - \frac{1}{(n\beta)^2}\right), \tag{2.2}$$

in which Z is the charge number of the particle and α is the fine structure constant. These properties of the Cherenkov radiation are very useful from the experimental point of view, and various types of the Cherenkov detectors have been used in experiments.

One type of these detectors is the threshold type Cherenkov detector. The HIRAC detector, described in this thesis, belongs to this type. A detector of this type usually consists of a radiator of a refractive index n, light guides, and photon detectors. Since only particles faster than the threshold velocity $\beta = 1/n$ emit Cherenkov photons in the radiator, this detector can distinguish whether the velocity is above or below the threshold velocity. Therefore, if the momentum of the coming particles is known or limited, particle identification on hardware level can be provided by choosing an appropriate refractive index of the radiator.

For radiators, various materials can be used. Typical materials and their refractive indices are listed in Table 2.1. Gases have refractive indices below 1.001, and liquids and solids have indices larger than 1.3. For the intermediate region between the gases and the liquids, silica aerogels can be used.

TABLE 2.1: Examples of materials and their refractive indices. The indices for gases are at the standard temperature and pressure (STP). The values are taken from Tabata *et al.*[17] for silica aerogel, Kleinknecht [18] for glass, and Beringer *et al.*[19] for other materials.

Material	Refractive index	Material	Refractive index
H_2 gas	1.000132	C (diamond)	2.42
D_2 gas	1.000138	Si	3.95
He gas	1.000035	Acrylic	1.49
N_2 gas	1.000298	Polystyrene	1.59
O_2 gas	1.000271	Polyvinyltoluene	1.58
F_2 gas	1.000195	Sapphire	1.77
Ne gas	1.000067	Glass	1.46 - 1.75
F_2 gas	1.000195	SiO_2	1.46
CO_2 gas	1.000449	Water	1.33
Ar gas	1.000281	Silica aerogel	1.0026 - 1.26
Xe gas	1.000701		

2.2 Design of the Detector

We have developed a high-refractive-index aerogel Cherenkov detector (HIRAC) consisting of an aerogel radiator, mirrors, and photomultiplier tubes (PMTs). In this section, the detail of each component is described.

2.2.1 Radiator

For the Cherenkov radiator, we adopted a silica aerogel with a refractive index of $n = 1.18$. This index corresponds to the threshold velocity for the Cherenkov radiation of $\beta = 0.847$, which is slightly above the velocity range of the signal deuterons, as shown in Figure 1.4. Since the number of Cherenkov photons emitted in unit length is proportional to $(1 - 1/(n\beta)^2)$, this large index is advantageous to get maximum light yield.

The aerogel was developed by a new method, called a pinhole drying method [17, 20]. In the conventional method, a silica aerogel is produced by three steps: alcogel synthesis, hydrophobic procedures, and supercritical drying. The refractive index of the final aerogel is determined by the alcogel synthesis, but in this step it has been limited practically up to 1.06. In the new method, after the synthesis of $n \sim 1.06$ alcogel and before moving to the second step, a pinhole drying process is newly introduced. In this process, the alcogel is placed in a container sealed except for small holes. Then, organic molecules are gradually evaporated, and shrinkage of the piece occurs as shown in Figure 2.1. During this this shrinkage, its refractive index increases, and the transmittance also increases. Figure 2.2 is a picture of a pinhole-dried aerogel and one without pinhole drying. The increase of the transmittance can be seen. Figure 2.3 shows a plot of refractive indices and transmission lengths of aerogels. As shown in this plot, by this new method, the refractive index of aerogel has been extended up to around 1.25 keeping sufficient transmittance.

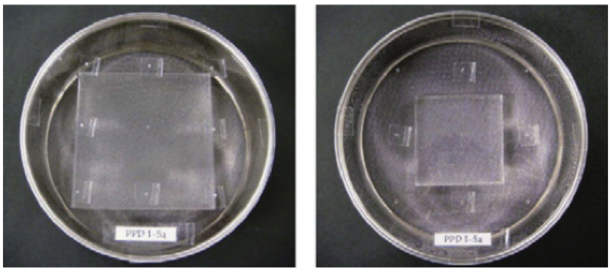

FIGURE 2.1: Shrinkage during the pinhole drying process. The left is before and the right is after this process. These pictures are taken from Adachi *et al.* [20].

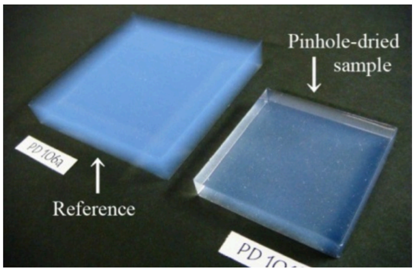

FIGURE 2.2: A picture of pinhole-dried aerogel (right) and one without pinhole drying (left). This picture is taken from Tabata *et al.*[17].

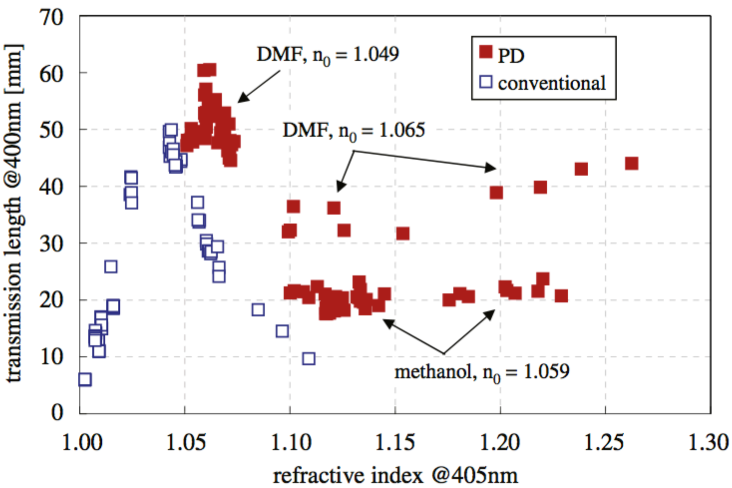

FIGURE 2.3: A plot of transmission lengths and refractive indices of aerogels. This figure is taken from Adachi *et al.* [20]

The refractive index was measured at three wavelengths as shown in Figure 2.4. To estimate the behavior of the refractive index from the ultraviolet region to the red region, the measured refractive indices were fitted by two empirical functions as

$$(n(\lambda))^2 = 1 + \frac{0.378\,\lambda^2}{\lambda^2 - (1.0\times 10^2\,\text{nm})^2}, \tag{2.3}$$

$$n(\lambda) = 1 + 0.174\left(1 + \left(\frac{1.0\times 10^2\,\text{nm}}{\lambda}\right)^2\right). \tag{2.4}$$

The transmittance in 1cm of the aerogel was measured from 200 nm to 800 nm by 0.5 nm step. At $\lambda = 400$ nm, it is around 0.65, which corresponds to about 2 cm in transmission length.

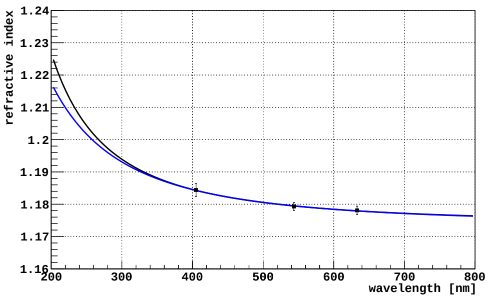

FIGURE 2.4: Wavelength dependence of the refractive index. The fitted function (2.3) is shown by a black curve, and (2.4) is shown by a blue curve.

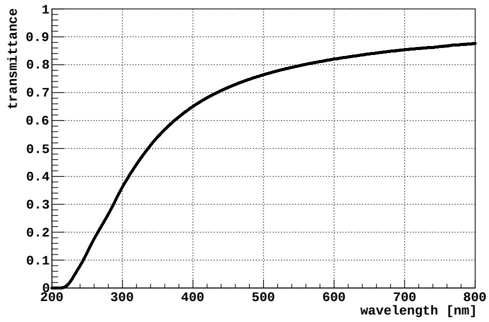

FIGURE 2.5: Wavelength dependence of the transmittance.

In the main experiment, an aerogel covering a large area of 270 mm in horizontal length and 90 mm in vertical length is necessary to cover the dispersive focal plane. As for the thickness, since the transmission length of this aerogel is about 2 cm, we chose the aerogel thickness to be 2 cm. However, because a size of one piece of the aerogel was limited for practical reasons, we placed 20 pieces of the aerogel into an aluminum box in two layers. We arranged them into the aluminum box alternately, as shown in Figure 2.6, so that gaps between the pieces in the first layer did not overlap those in the second layer. Then, these pieces placed in the box are supported softly by the four strings seen in Figure 2.7.

The spectrum of the Cherenkov photons from this 2 cm-thick aerogel is shown by the blue line in Figure 2.8. The Cherenkov emission spectrum (2.2) with the refractive index estimated by Equation (2.4), the transmittance in the aerogel (Figure 2.5), and the loss at the aerogel surface (Fresnel formula) were taken into account. The incident velocity was assumed to be $\beta = 0.95$. The rapid decrease in the short wavelength is due to the transmittance of the aerogel, and the decrease in the long wavelength is by the Cherenkov emission spectrum. The spectrum including the quantum efficiency of

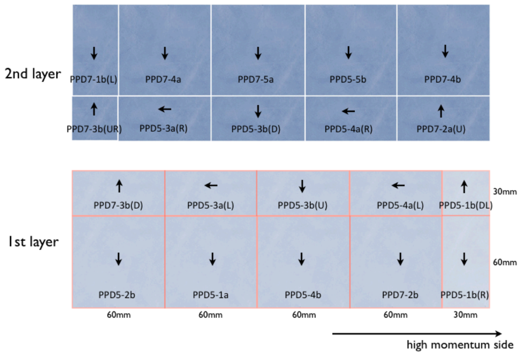

FIGURE 2.6: Arrangement of the aerogel pieces.

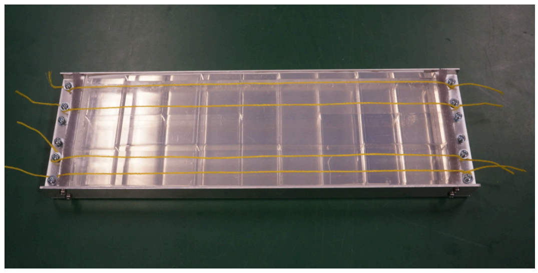

FIGURE 2.7: A picture of the aerogel box.

PMTs is shown by the red line. From this spectrum, the wavelength region of interest was deduced to be 250 nm – 600 nm.

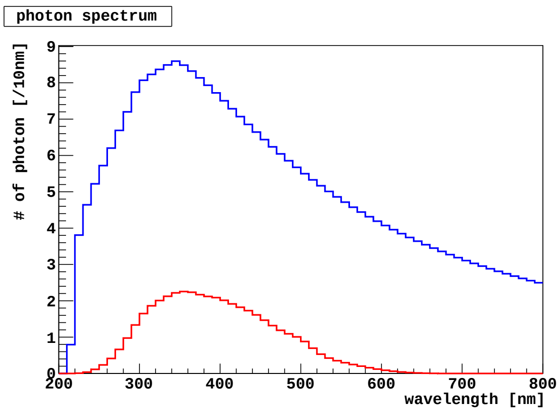

FIGURE 2.8: Calculated spectra of the Cherenkov photons and the photoelectrons are shown. The blue histogram is the spectrum of the Cherenkov photons from the 2 cm-thick aerogel, and the red histogram is the spectrum of the photoelectrons.

2.2.2 Mirror Box and Photomultipliers

In back of the radiator, a box consisting of an eight-plane mirror was placed to guide Cherenkov photons to photomultipliers attached on the top and bottom of the mirror box. Figures 2.9 and 2.10 show this structure. In this box, in front of the mirror planes, the aerogel box can be installed as illustrated in Figure 2.10.

The mirror is made of aluminum, and its surface is coated by MgF_2 layeres to prevent oxidation. The reflectance was measured at two incident angles, 5° and 45°, as shown in Figures 2.11 and 2.12. Dimensions of the mirrors are given in Figure 2.9. This configuration of the mirror plane was determined so that the performance is optimized, as described in section 2.3.

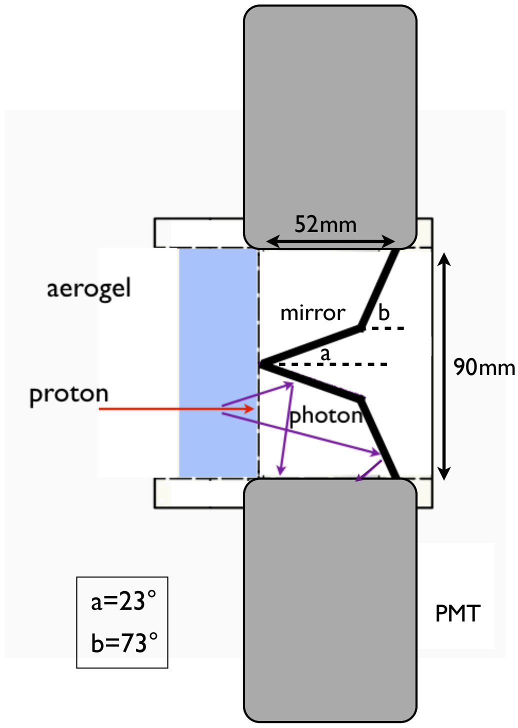

FIGURE 2.9: A side view of the mirror box.

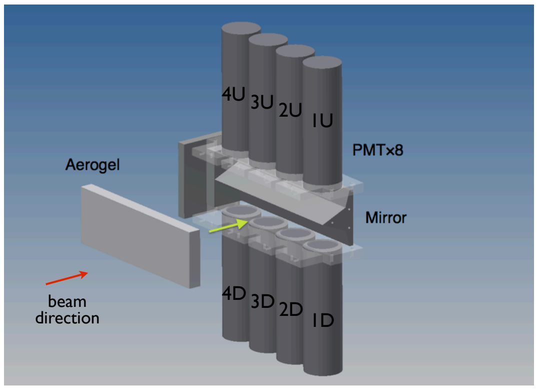

FIGURE 2.10: An overview of HIRAC. The aerogel box can be installed from the upstream side.

The Cherenkov photons reflected by the mirror planes are detected by eight PMTs equipped on the top and bottom of the mirror box. They are labeled as 1U, 2U, $\cdots$ 4D, as shown in Figure 2.10. For the PMTs, we used the type H6410 (Hamamatsu Photonics), in which the photomultiplier R329-02 is used. This is a two-inch PMT with twelve dynodes, and the front window is made of borosilicate glass, which is transparent at wavelengths longer than about 300 nm. The quantum efficiency of the PMT including transparency of the window is shown in Figure 2.13.

2.2.3 Entire Structure

The aerogel box, the mirror box, and the PMTs were placed in an outer box, as shown in Fig. 2.14. Inside this outer box, nitrogen gas was filled in order to keep the aerogel dry. The surface of the outer box was well sealed to prevent the nitrogen gas from leaking and outside light from entering the inside. In addition, the surface was painted in black color so that photons escaped from the mirror box can be absorbed by the inner surface of the outer box.

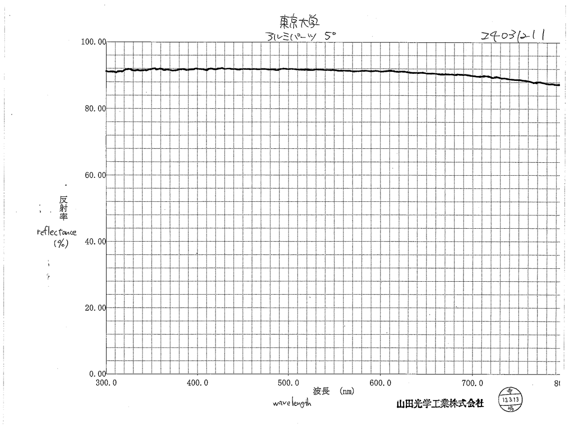

FIGURE 2.11: Reflectance of the mirror at incident angle 5°.

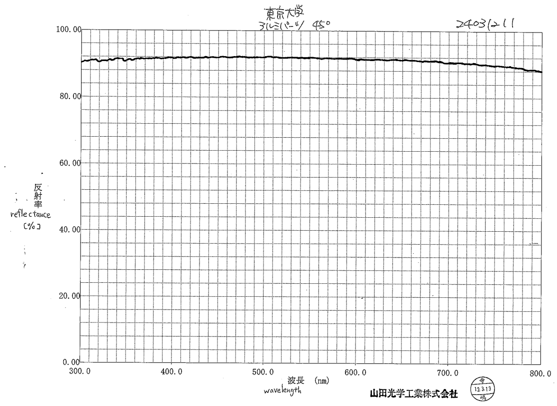

FIGURE 2.12: Reflectance of the mirror at incident angle 45°.

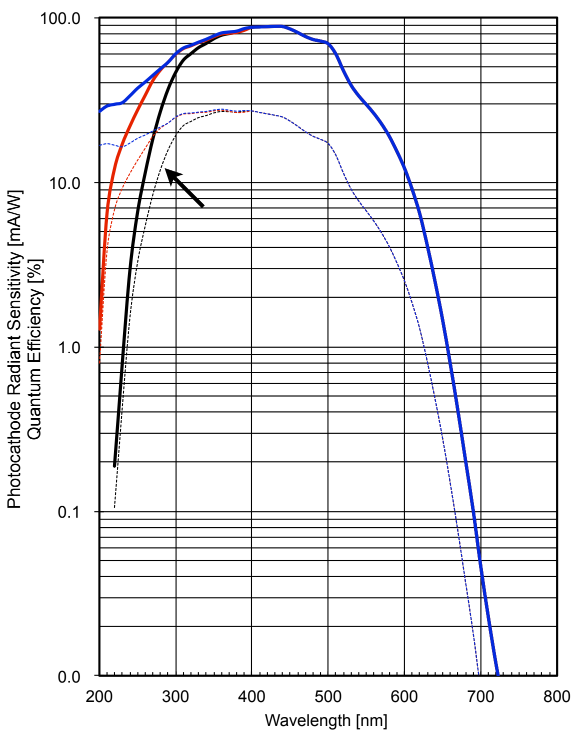

FIGURE 2.13: The quantum efficiency of the PMT (pointed by the arrow). In this graph, the transparency of the window is included. This figure is provided by Hamamatsu Photonics [21].

FIGURE 2.14: A picture of the outer box. This is a view from the upstream side without its front panel.

2.3 Optimization by Simulation

2.3.1 Concept

We simulated emission, propagation, and detection of the Cherenkov photons in order to optimize the configuration of the mirrors. In this simulation, the shape of the mirrors shown in Figure 2.9 was considered, and parameters optimized were two angles (a, b) of the mirrors.

In the following explanation, x is the horizontal axis, and y is the vertical axis. z is the beam axis, which is normal to the aerogel surface. The origin of the coordinate is taken at the center of the aerogel surface.

To determine the angles (a, b), we adopted the following criterion. By gridding the incident position (x, y) of the background proton at the surface of aerogel, we simulated the average number μ of photoelectrons detected by the eight PMTs for each (x, y) on the grid. Then, we chose the mirror angles where the minimum value of μ in the region of interest ($|x| \leq 135$ mm and $|y| \leq 30$mm) was maximized.

2.3.2 Calculation Method

The calculation was done in the following way.

1. First, mirror angles (a, b) to be considered were taken.

2. Secondly, incident beam conditions were defined. The velocity β and the incident angles (x', y') were fixed to $\beta = 0.95$ and $(x', y') = (0, 0)$. The incident position at the surface of the aerogel (x, y) was taken from $(-135\text{mm} \leq x \leq 135\text{mm}, -45\text{mm} \leq y \leq 45\text{mm})$.

3. The next step was to calculate the average number of photoelectrons ΔN attributed to Cherenkov photons emitted from the beam position between z and $z + \Delta z$, to the azimuthal angle from ϕ to $\phi + \Delta\phi$ corresponding to the beam axis, at the wavelength between λ and $\lambda + \Delta\lambda$. This ΔN was given by

$$\begin{aligned} \Delta N = \left(\frac{d^2 N}{dz d\lambda}\right) \Delta z \Delta\lambda \left(\frac{\Delta\phi}{2\pi}\right) &\times (\text{transmittance inside aerogel}) \\ &\times (\text{transmittance at aerogel surface}) \\ &\times (\text{whether this photon reach PMT(1) or not (0)}) \\ &\times (\text{reflectance of mirror})^{(\text{reflection times})} \\ &\times (\text{quantum efficiency of PMT}). \end{aligned} \tag{2.5}$$

For the refractive index $n(\lambda)$, the fitted function (2.4) was used. The transmittance inside the aerogel was calculated as $(\text{transmittance in 10 mm})^{(\text{length in aerogel})/10\,\text{mm}}$, using the data for 10 mm shown in Figure 2.5. The transmittance at the aerogel surface was calculated by the Fresnel equation. The next term, at the third line in (2.5), was calculated by simulation, taking into account refraction at the surface of aerogel and reflection by the mirrors. If a photon reached one of the photocathodes before entering the aerogel again, 1 was taken. For the reflectance of the mirror, to avoid overestimation, an uniform value of 85% was used. The last term, the quantum efficiency of the PMT was taken from Figure 2.13, taking into account incident-angle dependence of the transmittance in the window and the effective photocathode size.

4. The calculation 2. was repeated for 0 mm $\leq z \leq$ 20 mm, 200 nm $\leq \lambda \leq$ 800 nm, and $0 \leq \phi < 360°$ by step sizes of 1 mm , 1°, and 10 nm, respectively. Then, by summing up all contributions of ΔN, the average number of photoelectrons $\mu(x, y)$ for the incident beam position (x, y) was obtained.

5. By repeating 3. and 4. for every (x, y) in $(-135 \leq x \leq 135, -45 \leq y \leq 45)$ by 1 mm step, $\mu(x, y)$ was obtained for each position (x, y).

6. Then, the minimum value $\mu_{\rm min}$ was searched in the region of interest ($|x| \leq 135$ mm and $|y| \leq 30$ mm).

7. The procedures from 2. to 6. were repeated for each mirror angles (a, b) to be tested by 1° step. Then, we adopted the angles (a, b) where $\mu_{\rm min}$ was maximized.

2.3.3 Results

As a result of the calculations, the mirror angles which maximizes $\mu_{\rm min}$. were determined as $a = 23°, b = 73°$. With these angles, the distribution of $\mu(x, y)$, the average number of photoelectrons for an incident position (x, y) at the surface of the aerogel, is shown in Figure 2.15. The periodic pattern in x direction is due to the arrangement of the PMTs. Near the edges of $x = \pm 135$ mm, the numbers are decreasing because of the additional reflection by the side mirrors at $x = \pm 135$mm. In this figure, the minimum value in the region of interest is 12.7 at $(x, y) \sim (\pm 100\text{mm}, \pm 15\text{mm})$, and the average in the region of interest is 16.6.

2.4 Expected Performance

We estimated the rejection capability for several thresholds for the number of photoelectrons, for the poisson distribution with the average of μ =12.7 and 16.6. The result is shown in Table 2.2. In this table, a threshold of n p.e. means events with n or more than n photoelectrons are rejected. When at least μ =12.7 photoelectrons are expected, 99.5 % rejection capability can be achieved by setting the threshold at 5 photoelectrons.

For the determined angles, response to variation of incident velocity β and angle (x', y') was estimated. The calculations were done similarly, and results are shown in Table 2.3. In case of $\Delta\beta = -0.01$, decrease of 17 % is seen, but still this $\mu_{\rm min}$ is sufficient to achieve

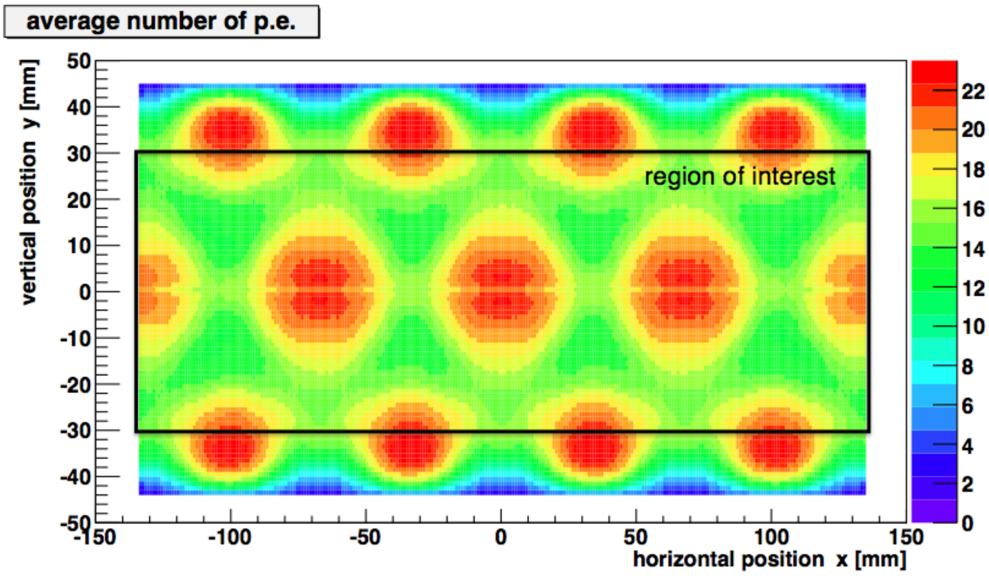

FIGURE 2.15: The average number of photoelectrons for the proton entering the aerogel at (x, y). The minimum value in the region of interest is 12.7 at $(x, y) \sim (\pm 100\text{mm}, \pm 15\text{mm})$.

TABLE 2.2: Rejection capability for $\mu = 12.7$ and 16.6.

threshold	rejection capability (μ=12.7)	rejection capability (μ=16.6)
3 p.e.	99.97 %	99.9990 %
4 p.e.	99.87 %	99.9943 %
5 p.e.	99.53 %	99.975 %
6 p.e.	98.7 %	99.91 %
7 p.e.	96.9 %	99.73 %
8 p.e.	93.7 %	99.30 %
9 p.e.	88.6 %	98.4 %

99.5% rejection capability. In the other cases in Table 2.3, no significant decrease of μ_{min} is seen.

It is noted that in the calculation described in 2.3.2, to avoid overestimation, some parts were being underestimated or neglected. For example, (1−(transmittance)) of

TABLE 2.3: Response to variation of the incident beam.

variation	change of μ_{min}
$\Delta\beta = +0.01$	-3%
$\Delta\beta = -0.01$	-17%
$\Delta x' = \pm 19\text{mrad}$	-1%
$\Delta y' = \pm 13\text{mrad}$	-2%

photons were killed in the calculation, but in reality some of these photons may be just scattered by small angles and reach the PMT. Also photons re-entering aerogel were regarded as disappeared, but they may be reflected several times by the inner surface of the aerogel box and finally reach the PMT. These contributions were not taken into account in the calculation. Therefore, in realistic case, more photons than the simulation are expected.

Chapter 3

Test Experiment

3.1 Overview of the Test Experiment

We performed a test experiment of the HIRAC detector using deuteron beams at GSI. We employed the deuteron beams of two different velocities, higher and lower than the Cherenkov threshold velocity, to evaluate background rejection capability and signal overkill probability of HIRAC in the main experiment. Furthermore, as seen in the calculation results (Figure 2.15), the HIRAC detector may have position dependence due to its geometrical structure like the positions of the PMTs. Therefore, such position dependence was also investigated by changing the HIRAC position. In this chapter, the details of the test experiment are described.

3.2 Facilities in GSI

The test experiment was performed at GSI laboratory. Figure 3.1 shows the facilities in GSI. A wide range of ions from proton to uranium can be accelerated by the linear accelerator (UNILAC) and further accelerated by the synchrotron (SIS). The maximum energy is 2 GeV/u for heavy ions, 3.9 GeV for deuterons, and 4.5 GeV for protons. After the acceleration by SIS, they are delivered to the experimental areas, such as the Fragment Separator (FRS), the Experimental Storage Ring (ESR), and the target halls (Cave A, B, and C).

The test of the HIRAC detector was carried out at Cave B. In Cave B, a large detector system of the FOPI experiment was located in the upstream side. Therefore, our detectors for the HIRAC test was installed at the downstream area of Cave B.

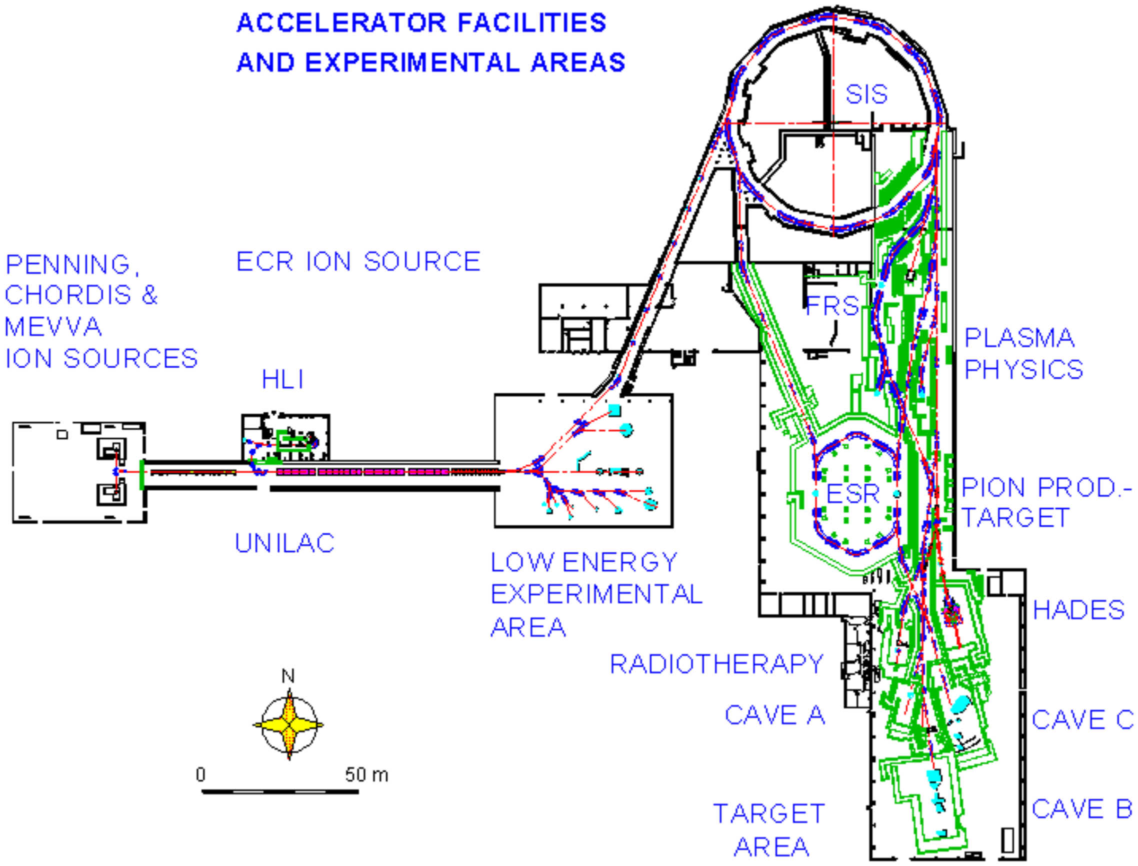

FIGURE 3.1: Facilities in GSI are shown.

3.3 Beam Conditions

We employed deuteron beams of two conditions: kinetic energy of 1900 MeV/u and 800 MeV/u, in order to simulate both the background protons and the signal deuterons in the main experiment. Table 3.1 shows these two conditions.

TABLE 3.1: Beam conditions used in the HIRAC test are shown.

type	beam energy	velocity ($\beta = v/c$)	spill length / period	intensity
background	1900 MeV/u	0.944	5 s / 10 s	0.5 - 5 MHz
signal	800 MeV/u	0.843	5 s / 10 s	1 MHz

The deuterons of 1900 MeV/u have the velocity of $\beta = 0.944$, which is in the velocity range of the background protons in the main experiment, as shown in Table 1.1. With this beam condition, background rejection capability of HIRAC was evaluated.

On the other hand, the deuterons of 800 MeV/u have the velocity of $\beta = 0.843$. This velocity is within the velocity region of the signal deuterons, corresponding to the η' binding energy of 90 MeV. If HIRAC detects photons for this velocity, it will result in signal overkill in the main experiment. Such signal overkill probability was evaluated with the second beam condition.

The spill length of the beam was 5 seconds with a repetition period of 10 seconds, and the intensity was around 0.5 – 5 MHz at an upstream FOPI start counter for the higher-velocity beam and about 1 MHz for the lower-velocity beam. When the intensity was higher than about 3 MHz, large gain fluctuation of the PMTs and many pile-up events were observed.[1] Therefore, only runs of the intensity lower than 3 MHz were used in analysis. The details of the run conditions are summarized in section 3.7.

3.4 Setup of the Detectors

Detectors for testing HIRAC were installed at the downstream area of Cave B. A schematic view of the setup is drawn in Figure 3.2. In the upstream area, a 1 mm-thick lead target was placed inside the FOPI detector,[2] and the setup for the HIRAC test was starting at 6.7 m behind the lead target.

3.4.1 Scintillators

Two finger counters were set in front of HIRAC to define positions of the incident deuterons. In Table 3.2, the size of the scintillators and the types of the PMTs are shown. To make the finger counter, a scintillator made of plastic and its support was mounted on the PMT window coated by optical grease. Then, the scintillator, the support, and the window of the PMT was covered by a black sheet to prevent contamination of outside light. We denote the one horizontally placed by Finger H, and the other one, standing upright, by Finger V.

Another scintillation counter, SCI, was placed at the end of the setup. The size of SCI was 40 mm in width, 50 mm in hight, and 5 mm in thickness. This scintillator was used in the offline analysis to check whether the beam reaches the end.

[1] Another test of an RPC detector was performed in parallel. The very high-intensity beam was taken by request from this RPC test experiment.

[2] This lead target was installed for the RPC test as a scatterer. The RPC detector was installed off the beam axis and measuring scattered particles.

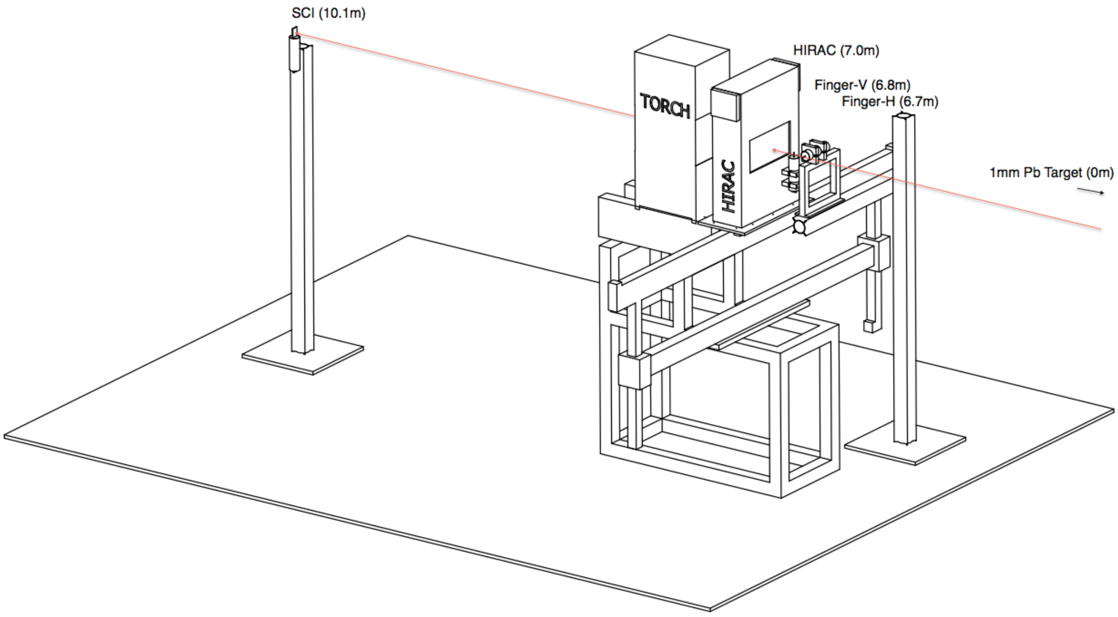

FIGURE 3.2: A setup of the detector is shown. The deuteron beam is coming from the right side. Numbers in parentheses are distances measured from the upstream lead target located inside the FOPI detector. TORCH is a detector tested at the same time, but not discussed in this thesis.

TABLE 3.2: Dimensions of the scintillators and types of the PMTs.

label	horizontal length	vertical length	thickness	PMT
Finger H	30 mm	3 mm	3 mm	H6522 (Hamamatsu)
Finger V	3 mm	30 mm	3 mm	H6522 (Hamamatsu)
SCI	40 mm	50 mm	5 mm	H2431(Hamamatsu)

3.4.2 HIRAC

HIRAC was installed behind the finger counters. It was placed on a movable stage to investigate its position dependence. This stage could be moved both horizontally and vertically by a remote control. During the experiment, dried nitrogen gas was filled inside HIRAC, and high voltage was applied to the inside PMTs. The setting of the high voltage is tabulated in Table 3.3.

TABLE 3.3: High voltage setting for HIRAC.

PMT label	1U	2U	3U	4U
high voltage	2475 V	2325 V	2275 V	2325 V
PMT label	1D	2D	3D	4D
high voltage	2150 V	2175 V	2200 V	2450 V

3.5 Data Acquisition Scheme

Signals of HIRAC and the scintillators were analyzed by TDC and QDC. Figure 3.3 shows a diagram of the data acquisition circuit. First, signals from HIRAC 1U, 2U, $\cdots$ 4D, and Finger H, Finger V, SCI were divided into a QDC branch and a TDC branch. Then, the QDC branches were delayed by 75 ns to fit in the QDC gate and connected to the QDC inputs. The TDC branches were discriminated, delayed by 200 ns, and connected to the TDC stops.

In addition, a diamond counter which is a start counter of the upstream FOPI detector was analyzed by the TDC. This signal was provided in NIM signal, so it was directly connected to the TDC stop. Also, a PMT without high voltage applied was analyzed by the QDC. This is denoted by common-mode noise in Figure 3.3. This was used in offline analysis for reducing a common-mode noise of low frequency observed.

For the trigger of the data acquisition, coincidence of Finger H and Finger V was used. The discriminated NIM signal of Finger H was delayed by 12 ns, and input to the coincidence module with the discriminated Finger V signal so that Finger H always defined the start timing of the TDC. Then, this coincidence was used to make the trigger, the QDC gate, and the common start of the TDC.

3.6 Calibrations

3.6.1 Gain Calibration

A gain calibration of each PMT was necessary to convert QDC values into the numbers of photoelectrons. For this calibration, we used attenuated LED light down to about one photoelectron for each PMT, and deduced the gain from the positions of a pedestal peak and a single-photoelectron peak. The setup is shown in Figure 3.4. We attached two blue LEDs inside the HIRAC detector. Then, for the input to the LEDs, random pulses discriminated, converted into TTL pulses, and attenuated were used. The width of the pulses and the strength of the attenuation were adjusted so that only a very few photoelectrons were detected by each PMT. The output of the discriminator was also used for the trigger after being delayed by 200 ns to compensate for the response time of the LED side. With this setup, we measured the gains of the PMTs before and after each beam time.

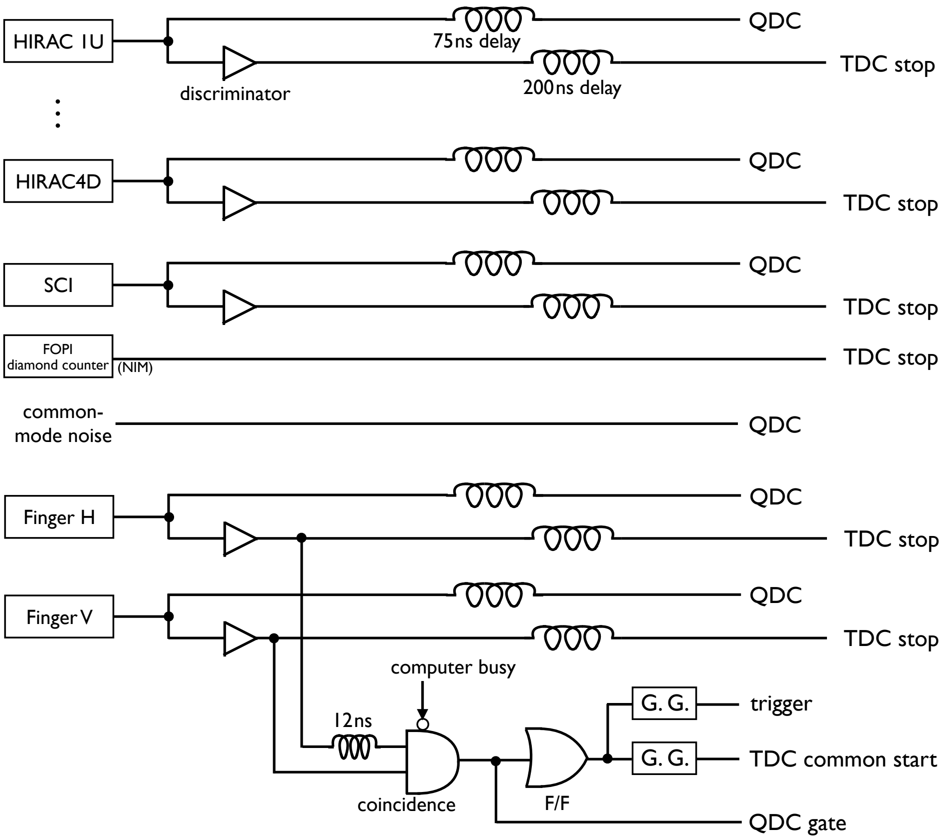

FIGURE 3.3: A data acquisition scheme is shown.

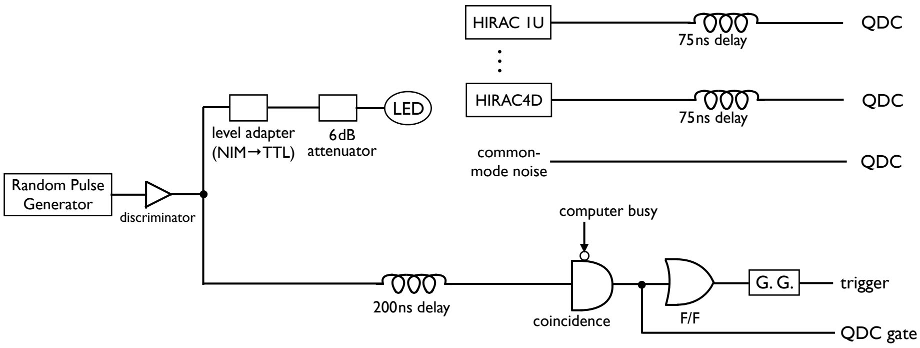

FIGURE 3.4: A setup for the gain calibration is shown.

3.6.2 TDC Calibration

TDC calibration was carried out to obtain time interval corresponding to one channel of the TDC. The setup is shown in Figure 3.5. We used a time calibrator module, which gives two NIM outputs: a start signal and a stop signal. The stop signal occurs at a random integral multiple of a selected time interval (20 ns) after each start signal. Therefore, obtained TDC histograms were like combs with an interval of 20 ns, and conversion factors from TDC channel to time were derived.

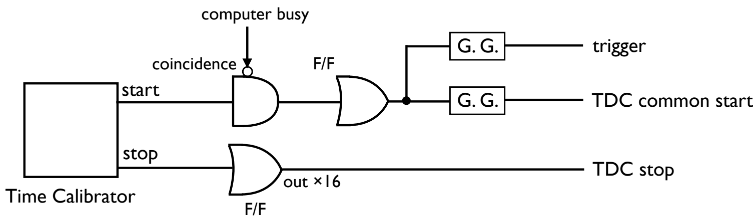

FIGURE 3.5: A setup for the TDC calibration.

3.7 Run Summary

We tested HIRAC with the setup described in this chapter using the two types of deuteron beams for two hours per day for two days. The run conditions are summarized in Table 3.4. Data were taken at four positions of HIRAC with the higher-energy deuteron and at twelve positions with the lower-energy deuteron.

Table 3.4: Summary of the run conditions. The runs with too high intensity, which could not be used in analysis, are omitted from this table.

Beam Energy	HIRAC position (x,y)	intensity
(gain calibration)	-	-
1900 MeV/u	(0 mm, 0 mm)	$\sim$0.5 MHz
1900 MeV/u	(16.9 mm, 0 mm)	$\sim$0.5 MHz
1900 MeV/u	(33.8 mm, 0 mm)	$\sim$0.5 MHz
1900 MeV/u	(0 mm, 10 mm)	$\sim$0.5 MHz
(gain calibration)	-	-
(gain calibration)	-	-
800 MeV/u	(0 mm, 0 mm)	$\sim$1 MHz
800 MeV/u	(101.3 mm, 0 mm)	$\sim$1 MHz
800 MeV/u	(101.3 mm, 10 mm)	$\sim$1 MHz
800 MeV/u	(101.3 mm, 20 mm)	$\sim$1 MHz
800 MeV/u	(120 mm, 10 mm)	$\sim$1 MHz
800 MeV/u	(120 mm, 0 mm)	$\sim$1 MHz
800 MeV/u	(0 mm, 0 mm)	$\sim$1 MHz
800 MeV/u	(33.8 mm, 0 mm)	$\sim$1 MHz
800 MeV/u	(67.5 mm, 0 mm)	$\sim$1 MHz
800 MeV/u	(0 mm, 10 mm)	$\sim$1 MHz
800 MeV/u	(33.8 mm, 10 mm)	$\sim$1 MHz
800 MeV/u	(33.8 mm, 20 mm)	$\sim$1 MHz
800 MeV/u	(16.9 mm, 0 mm)	$\sim$1 MHz
(gain calibration)	-	-
(TDC calibration)	-	-

Chapter 4

Analysis and Results

In this chapter, analysis and results of the test experiment are presented. The scheme of the analysis is the following.

1. Analysis of the PMT gain calibration and the TDC calibration was done.
2. Cut conditions for event selection were defined.
3. Under the conditions defined in 2., histograms of the total numbers of photoelectrons were obtained.
4. Relations of the efficiency and the threshold were obtained.

In the following sections, the details of these procedures are explained.

4.1 Calibrations

4.1.1 Gain Calibration

In the gain calibration runs, QDC histograms consisting of a pedestal peak and few-photoelectron components were obtained. As an example, a histogram of HIRAC 1D is shown in Figure 4.1. The black histogram shows a raw histogram obtained. Due to the common-mode noise, two peaks are seen in the pedestal. Figure 4.2 shows a two dimensional plot of this HIRAC channel and the empty channel (common-mode noise). Almost linear correlation between them is seen. Therefore, the QDC values can be corrected as

$$\mathrm{QDC}_{\mathrm{corrected}}(i) = \mathrm{QDC}(i) - f(i)(\mathrm{QDC}_{\mathrm{noise}} - \overline{\mathrm{QDC}_{\mathrm{noise}}}) \quad (i = 1\mathrm{U}, 2\mathrm{U}, \cdots 4\mathrm{D}), \quad (4.1)$$

where $f(i)$ is the slope of the correlation. The corrected histogram is shown by the red histogram in Figure 4.1.

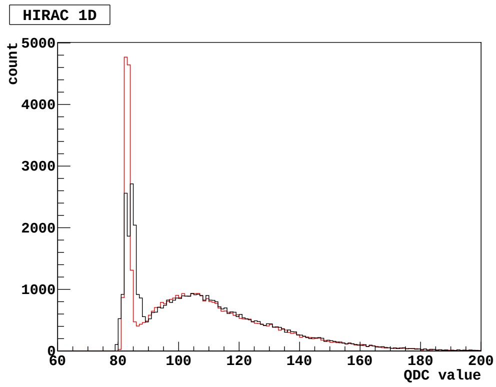

FIGURE 4.1: A QDC spectrum of PMT gain calibration. The black histogram is a raw histogram, and the red histogram is the corrected histogram.

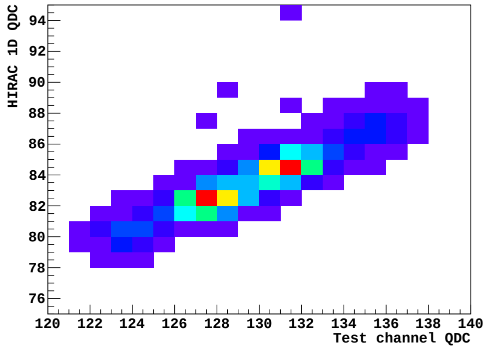

FIGURE 4.2: Correlation between QDC values of HIRAC 1D and the empty channel due to the common-mode noise.

To obtain gains of the PMTs, the corrected histograms were fitted by a function consisting of a pedestal peak and from one to five-photoelectron peaks. Each peak was assumed to be gaussian[1] with a standard deviation proportional to $\sqrt{n}$ for the n-photoelectron peak. The fitted parameters are the following ten parameters: a gain, a pedestal position, areas of six peaks, a standard deviation of the pedestal peak, and that of the one-photoelectron peak. Examples of the fitted functions are shown in Figure 4.3.

In analysis, we used the averaged value of the gains obtained in the two calibrations before and after the run. The values used for the first day and the second day are tabulated in Table 4.1. The errors are including errors of the fitting and uncertainties between the two calibrations before and after the run.

4.1.2 TDC Calibration

In the TDC calibration, histograms like combs were obtained, as shown in Figure 4.4. The intervals from peaks to the next peaks are equal to 20 ns, which is the interval time selected in the time calibrator. Then, we fitted each peak position by gaussian, and assigned time of $20(n-1)$ ns for the n-th peak. Figure 4.5 is the relation between the assigned time and peak channel. A good linearity is seen up to around 3000 channel,

[1] To be exact, the response function of PMT is not gaussian. It is mainly determined by a distribution of the electron multiplication at the first dynode. The gain of this PMT is about 10^7, which corresponds to 4 per dynode, at the high voltage of 2200 V [22]. If we assume the distribution at the first dynode is a poisson distribution with the average of 4, it is already like a gaussian distribution around the peak. Therefore, the assumption that each photoelectron peak is gaussian is approximately correct.

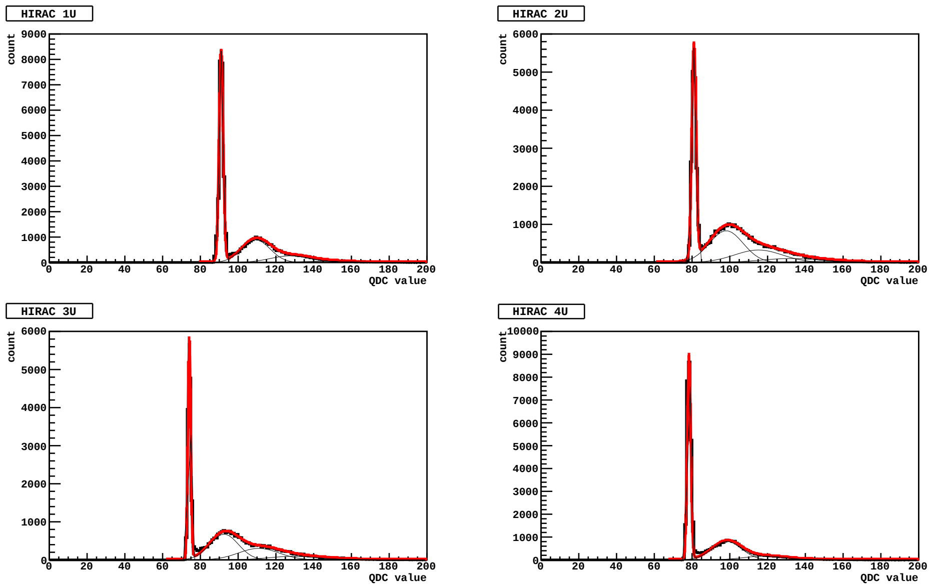

FIGURE 4.3: Examples of fitting gain calibration spectra for the upper PMTs. The red curves are the fitted functions, and the black curves are the components.

TABLE 4.1: Gains of the PMTs obtained by the gain calibration runs. These values are in QDC channels per photoelectron.

Day	1U	2U	3U	4U
1st day	18.2±0.3	16.9±0.5	18.0±0.2	19.7±0.2
2nd day	18.5±0.2	17.2±0.2	18.6±0.3	20.0±0.1

Day	1D	2D	3D	4D
1st day	15.6±1.1	18.3±0.4	14.0±0.7	18.6±0.4
2nd day	16.2±0.6	17.9±0.4	14.1±0.3	19.5±0.3

including the signal timing around 500 channel of HIRAC, Fingers, and SCI and around 1200 channel of the FOPI start counter. By fitting this plot linearly from 0 to 3000 channel, coefficients for converting TDC channel into time were derived as tabulated in Table 4.2.

TABLE 4.2: Time interval for one channel of TDC. These values are in ps per TDC channel.

1U	2U	3U	4U	1D	2D	3D	4D
299.9	305.6	310.9	307.0	309.6	309.8	309.0	307.3

Finger H	Finger V	SCI	FOPI start
306.0	305.7	303.6	304.5

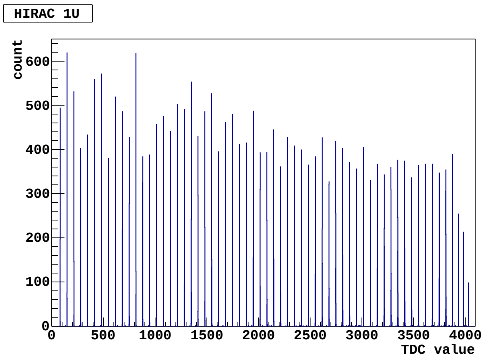

FIGURE 4.4: A histogram of the TDC calibration. The intervals from peaks to the next peaks are corresponding to 20 ns.

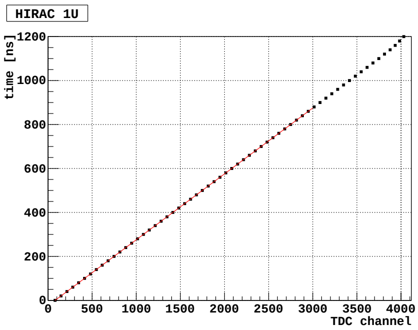

FIGURE 4.5: Linearity between TDC channel and time. This was fitted by a linear function as shown in the red line. the residual plot is shown in Figure 4.6.

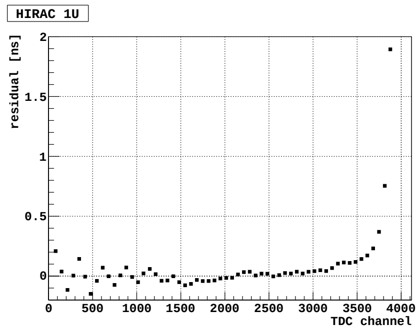

FIGURE 4.6: A residual plot of fitting the TDC linearity.

4.2 Event Selection

In order to select appropriate events, we defined conditions on QDC values and TDC values. First, Figure 4.7 and Figure 4.8 show correlations of QDC between Finger H and Finger V for the higher energy and the lower energy, respectively. To select the main component, we adopted cut conditions shown in black lines in these figures.

Secondly, the TDC correlations between Finger H and finger V are shown in Figure 4.9 for the higher-energy run and in Figure 4.10 for the lower-energy run. Finger V has broader distribution, because the signal of Finger H is defining the start timing of TDC. We adopted conditions to select the main peak as shown in these figures.

Next, cut conditions for QDC of SCI are shown in Figure 4.11 and 4.12. If the beam was coming straight, all particles except for scattered ones should have hit SCI. However, in the QDC spectrum, about a half of the events are at the pedestal position. This means that a considerable amount of particles in the triggered events had large incident angles. Therefore, we set the conditions and removed these events.

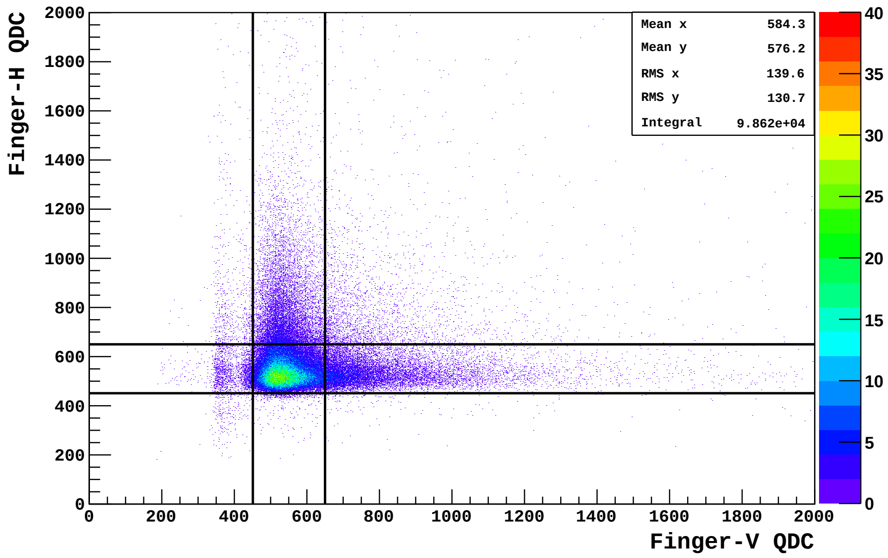

FIGURE 4.7: Cut conditions for Finger QDC for the higher-energy deuterons.

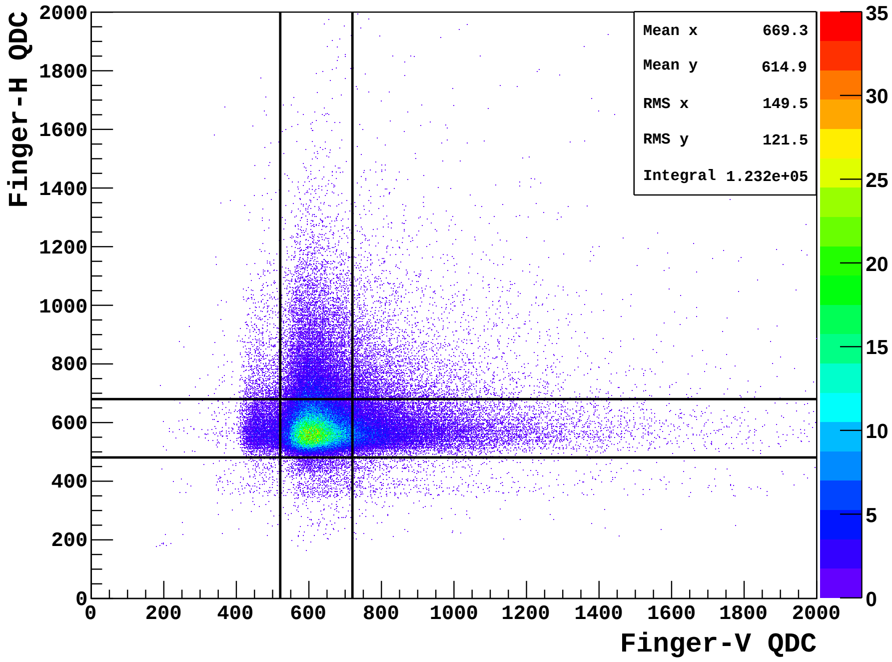

FIGURE 4.8: Cut conditions for Finger QDC for the lower-energy deuterons.

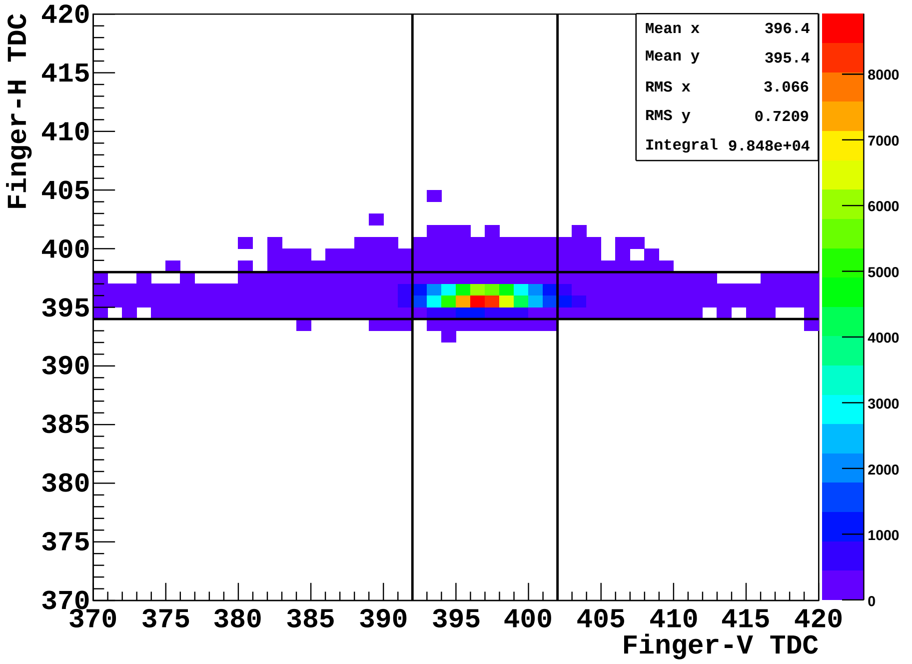

FIGURE 4.9: Cut conditions for Finger TDC for the higher-energy deuterons.

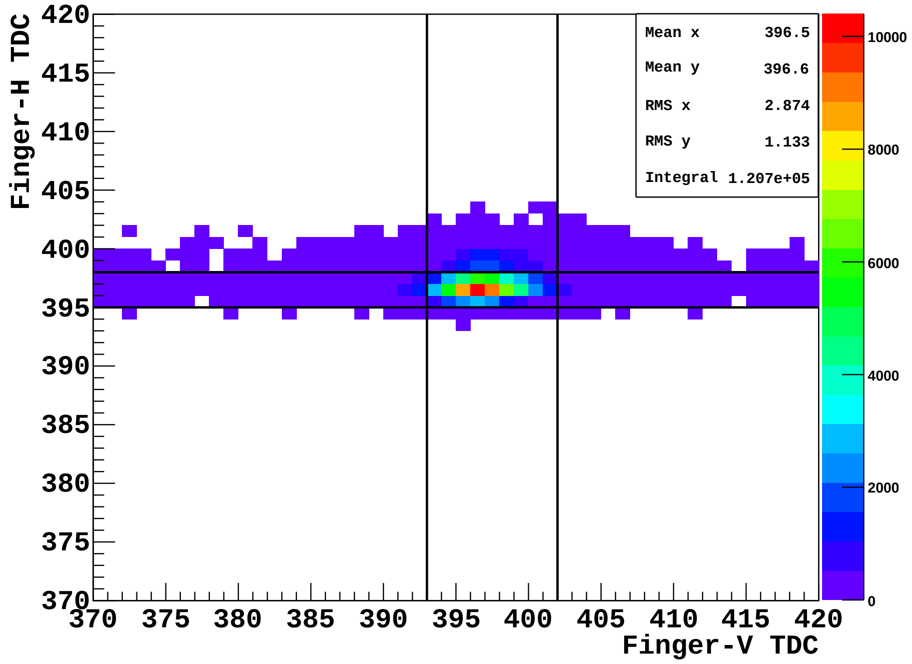

FIGURE 4.10: Cut conditions for Finger TDC for the lower-energy deuterons.

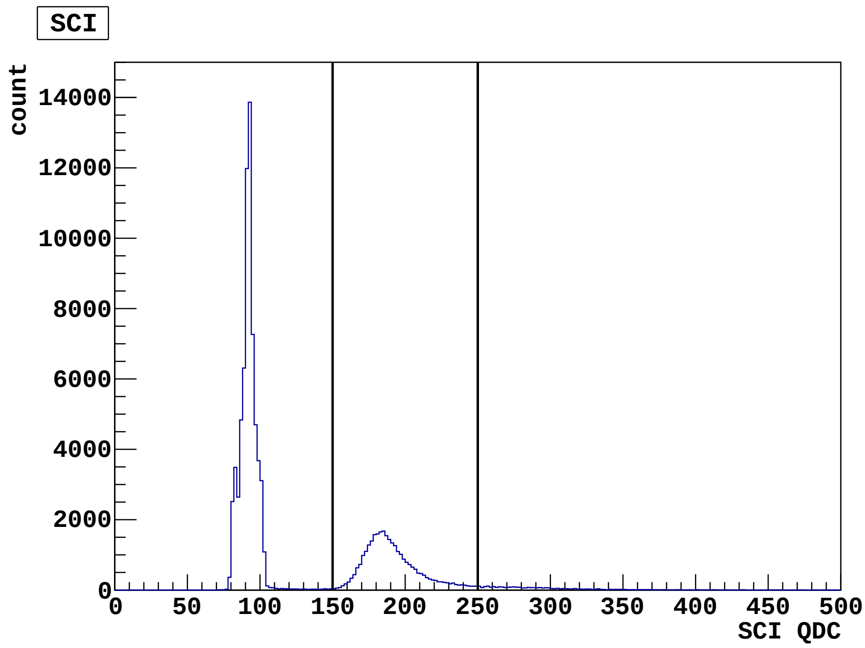

FIGURE 4.11: A cut condition for SCI QDC for the higher-energy deuterons.

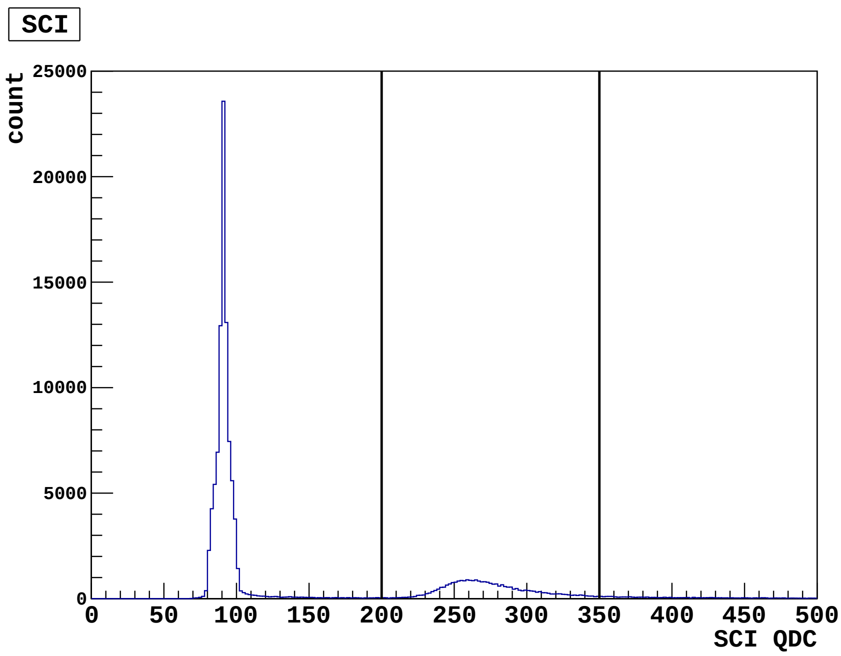

FIGURE 4.12: A cut condition for SCI QDC for the lower-energy deuterons.

In addition to the conditions on Finger H, Finger V, and SCI, we set a condition for the timing of the start counter to reduce multi-hit contribution in the lower energy runs. Figure 4.13 is the TDC histogram of the start counter. The timing of the triggered particles at this counter is at the peak around 1230 channel. Events before this peak are accidental particles coming before the triggered particles. By setting the condition at this peak, as shown by the black lines in the magnified histogram, at least multi-hit events with earlier accidentals can be reduced.

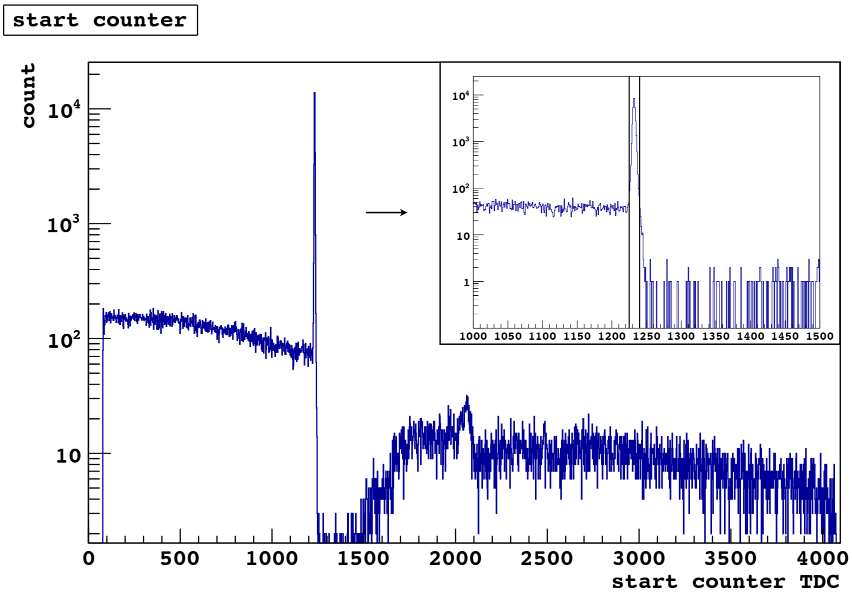

FIGURE 4.13: A cut conditions for TDC of the upstream start counter for the lower-energy deuterons.

4.3 Photoelectron Histogram

Under all the conditions described in section 4.2, histograms of the total number of photoelectrons are derived. The total number of photoelectrons was calculated as

$$(\text{total number of p.e.}) \quad = \sum_{i=\{1\mathrm{U},\ 2\mathrm{U},\cdots 4\mathrm{D}\}} \frac{\mathrm{QDC}(i)_{\text{corrected}} - \mathrm{QDC}(i)_{\text{corrected, pedestal}}}{\mathrm{Gain}(i)}, \qquad (4.2)$$

where Gain(i) is the gain obtained in the gain calibration.

4.3.1 Photoelectron Histogram for the Higher Velocity

Firstly, the histograms of the total number of photoelectrons for the higher-energy deuterons at the four incident positions to HIRAC are shown in Figure 4.14 - 4.17.

In all these cases, there are main peaks around 20 - 30 photoelectrons, and no events near the pedestal position are seen.

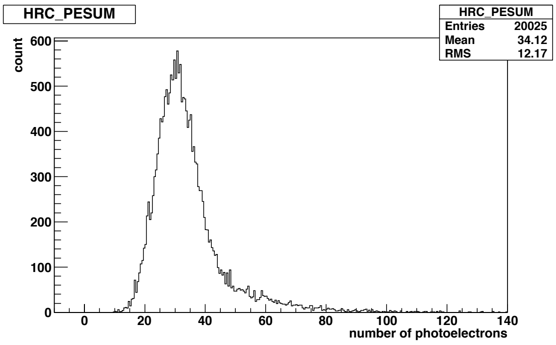

FIGURE 4.14: A histogram of the total number of p.e. for the higher velocity at an incident position (0 mm, 0 mm).

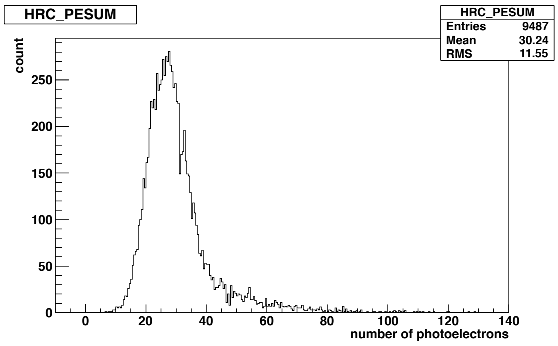

FIGURE 4.15: A histogram of the total number of p.e. for the higher velocity at an incident position (16.9 mm, 0 mm).

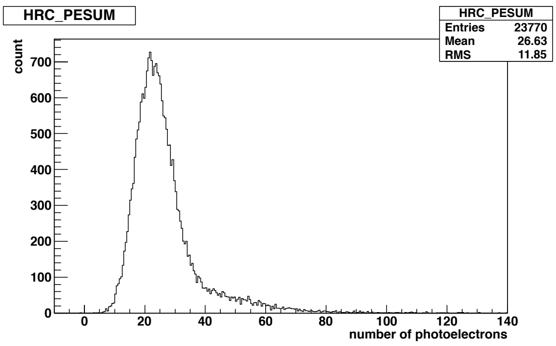

FIGURE 4.16: A histogram of the total number of p.e. for the higher velocity at an incident position (33.8 mm, 0 mm).

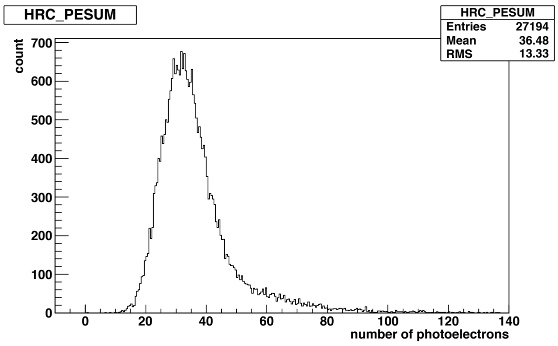

FIGURE 4.17: A histogram of the total number of p.e. for the higher velocity at an incident position (0 mm, 10 mm).

Then, these histograms were fitted by the following function in order to obtain the average numbers of photoelectrons.

$$f(x;\mu,A,\sigma_1) = A\sum_n \mathrm{Poisson}(n;\mu) \times \mathrm{Gauss}(x;n,\sigma_1\sqrt{n}), \qquad (4.3)$$

where $\mathrm{Poisson}(n;\mu)$ is the poisson distribution with average μ, and $\mathrm{Gauss}(x;n,\sigma)$ is the gaussian distribution with the average n and the variance σ^2. Fitted parameters were μ, A, and σ_1, and fitting region was taken from 0 to the peak position plus one sigma of the peak. Figures 4.18 - 4.21 show the fitted functions and their residual plots. Within this region, the fitted functions agreed well with the histograms.

However, on the higher side of the peak, there is excess of about 10 % of the total events. This excess may be because of multi-hit events. Although the counting rate of the upstream start counter measured by a visual scaler was about 0.5 MHz, effective rate could be several times higher due to a micro structure of the beam. Actually the probability of having at least one event in 80 ns of QDC gate can be estimated from the TDC histogram of the upstream start counter. As it has 8 - 11 % of events in 80 ns accidentally in the region before the main peak, it seems consistent to explain the excess by the multi-hit events.

By the fitting, average numbers μ of the poisson distribution were derived. Table 4.3 shows the average numbers obtained by the fitting and those by the simulation for $\beta = 0.944$. The first errors are resulting from the fitting, and the second errors are systematic errors due to the uncertainty of the PMT gains. In all the cases, the average numbers obtained are higher than the simulated values, probably because of the underestimations in the simulation, and these numbers are quite sufficient to achieve 99.5 % background rejection capability.

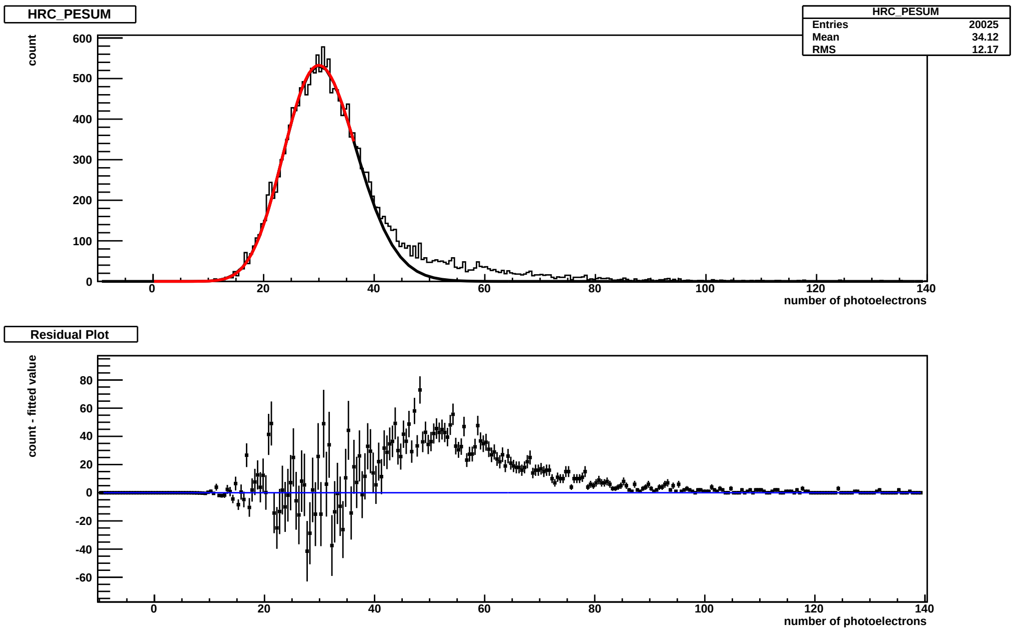

FIGURE 4.18: A result of fitting the photoelectrons histogram for the higher-energy deuterons at (0 mm, 0 mm). A residual plot is shown in the lower graph.

TABLE 4.3: The average numbers obtained by fitting and by simulation.

HIRAC position (x,y)	fitted average	simulated average
(0 mm, 0 mm)	30.8 ±0.1 ±0.5	22.1
(16.9 mm, 0 mm)	26.9 ±0.1 ±0.6	19.1
(33.8 mm, 0 mm)	23.2 ±0.1 ±0.3	13.8
(0 mm, 10 mm)	32.5 ±0.1 ±0.8	21.4

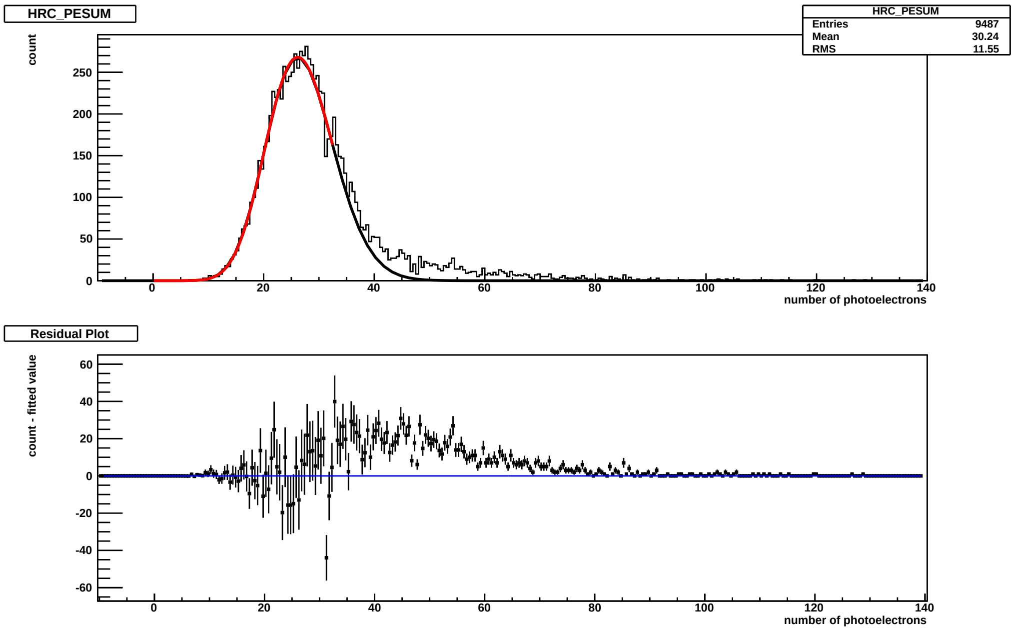

FIGURE 4.19: A result of fitting the photoelectrons histogram for the higher-energy deuterons at (16.9 mm, 0 mm). A residual plot is shown in the lower graph.

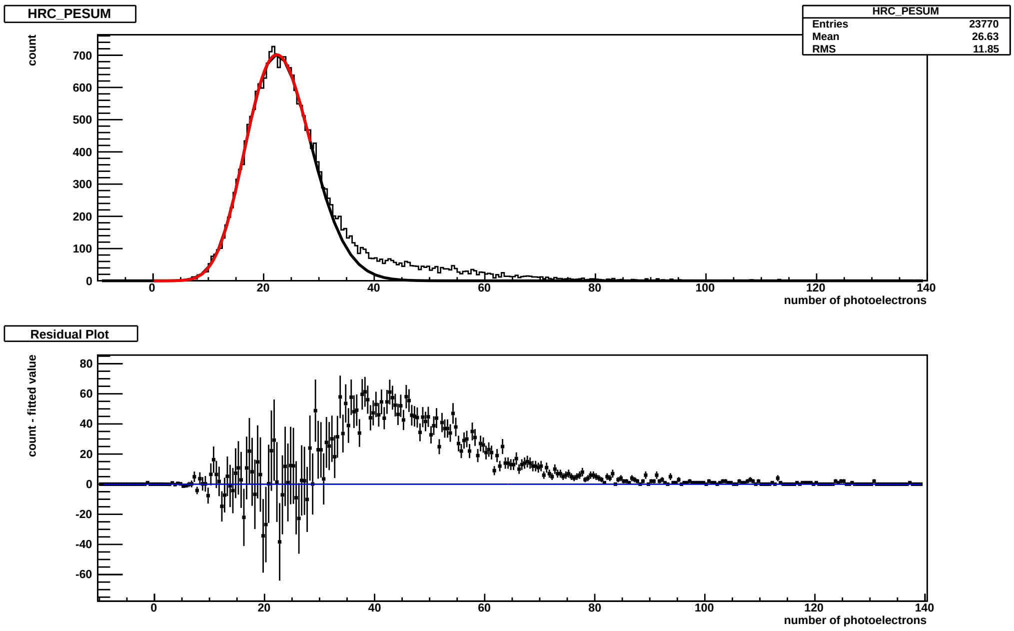

FIGURE 4.20: A result of fitting the photoelectrons histogram for the higher-energy deuterons at (33.8 mm, 0 mm). A residual plot is shown in the lower graph.

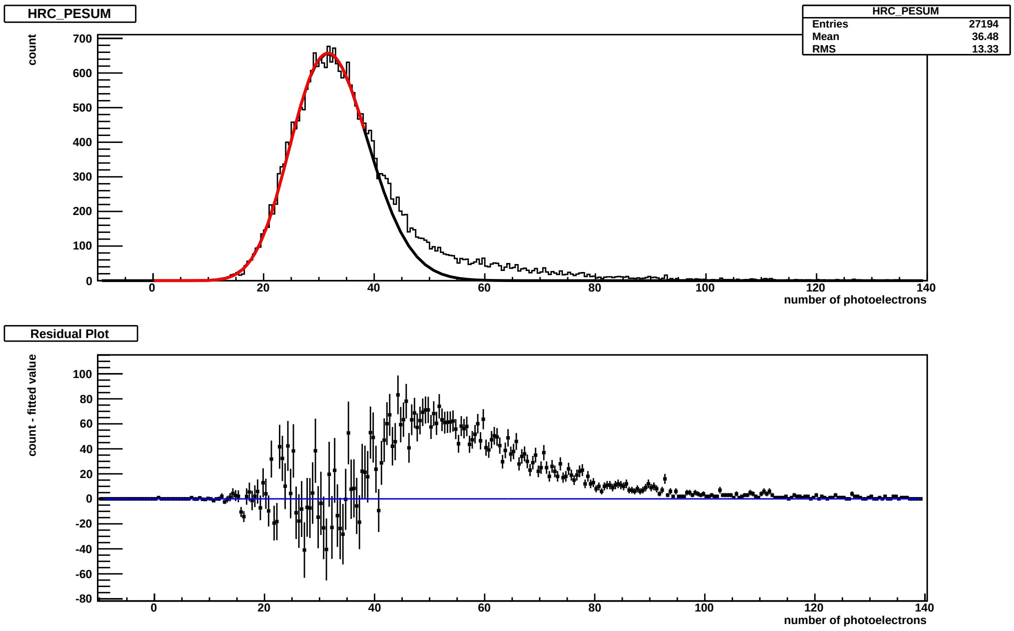

FIGURE 4.21: A result of fitting the photoelectrons histogram for the higher-energy deuterons at (0 mm, 10 mm). A residual plot is shown in the lower graph.

4.3.2 Photoelectron Histogram for the Lower Velocity

Next, histograms of the total numbers of photoelectrons for the lower-energy deuterons at twelve incident positions to HIRAC are shown in Figures 4.22 - 4.33. In all the cases, the main peak is at 0 photoelectron, as expected. However, tails up to more than 10 photoelectrons are also seen. These may raise signal overkill probability in the main experiment, as discussed in section 4.5.

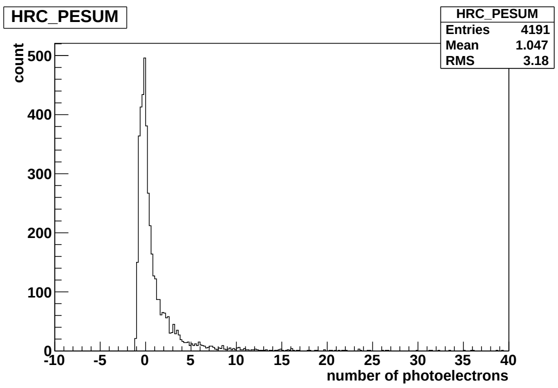

FIGURE 4.22: A histogram of the total number of p.e. for the lower velocity at an incident position (0 mm, 0 mm).

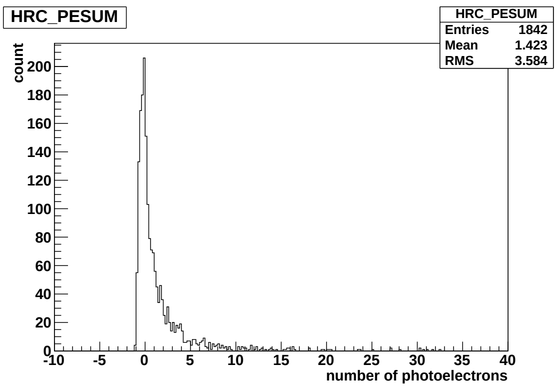

FIGURE 4.23: A histogram of the total number of p.e. for the lower velocity at an incident position (0 mm, 10 mm).

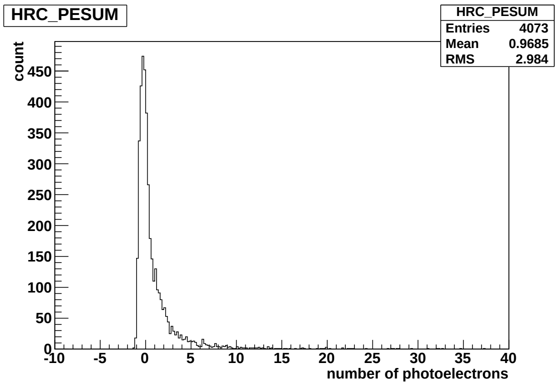

FIGURE 4.24: A histogram of the total number of p.e. for the lower velocity at an incident position (16.9 mm, 0 mm).

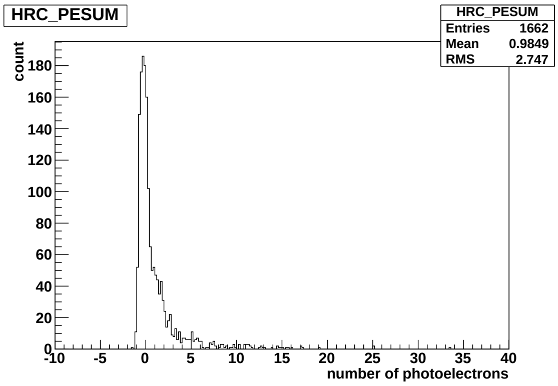

FIGURE 4.25: A histogram of the total number of p.e. for the lower velocity at an incident position (33.8 mm, 0 mm).

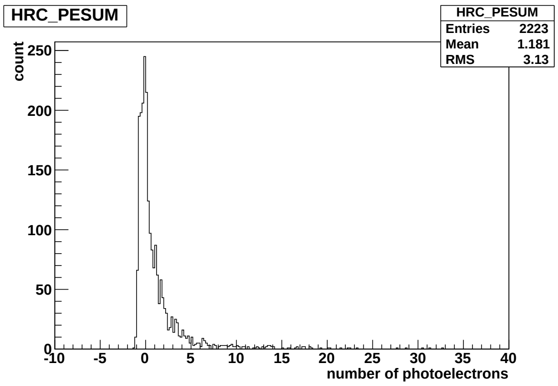

FIGURE 4.26: A histogram of the total number of p.e. for the lower velocity at an incident position (33.8 mm, 10 mm).

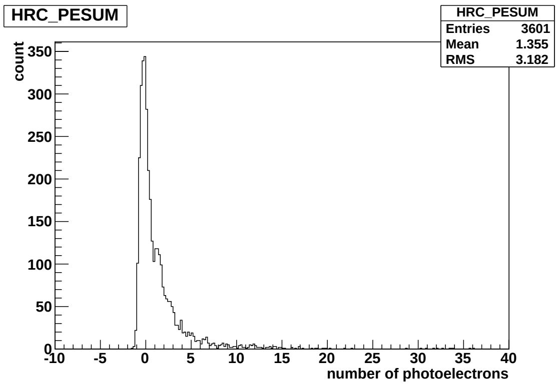

FIGURE 4.27: A histogram of the total number of p.e. for the lower velocity at an incident position (33.8 mm, 20 mm).

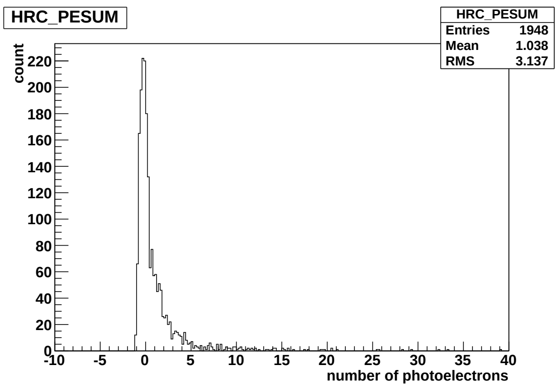

FIGURE 4.28: A histogram of the total number of p.e. for the lower velocity at an incident position (67.5 mm, 0 mm).

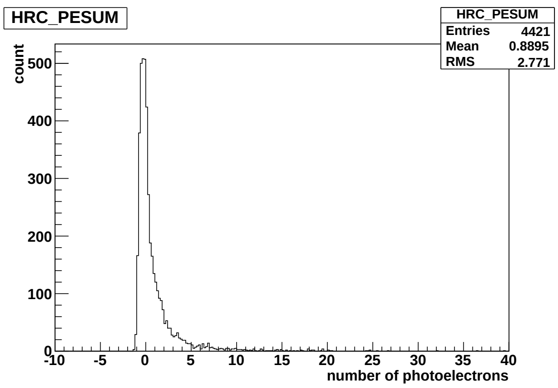

FIGURE 4.29: A histogram of the total number of p.e. for the lower velocity at an incident position (101.3 mm, 0 mm).

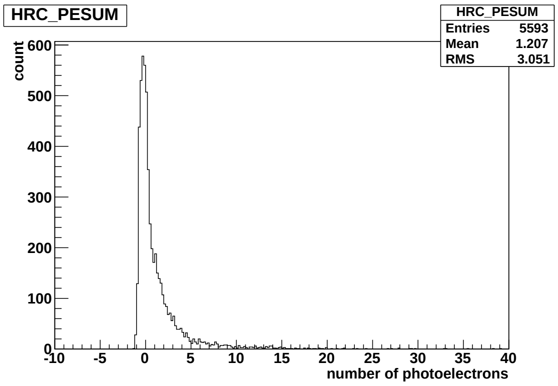

FIGURE 4.30: A histogram of the total number of p.e. for the lower velocity at an incident position (101.3 mm, 10 mm).

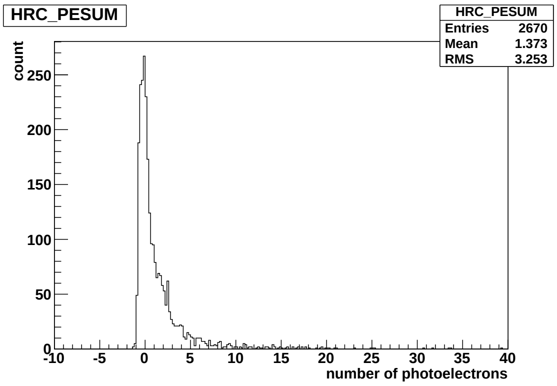

FIGURE 4.31: A histogram of the total number of p.e. for the lower velocity at an incident position (101.3 mm, 20 mm).

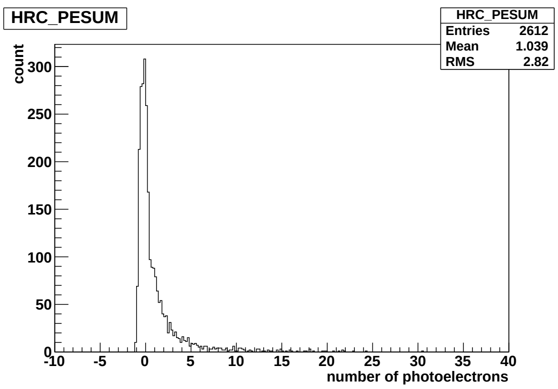

FIGURE 4.32: A histogram of the total number of p.e. for the lower velocity at an incident position (120 mm, 0 mm).

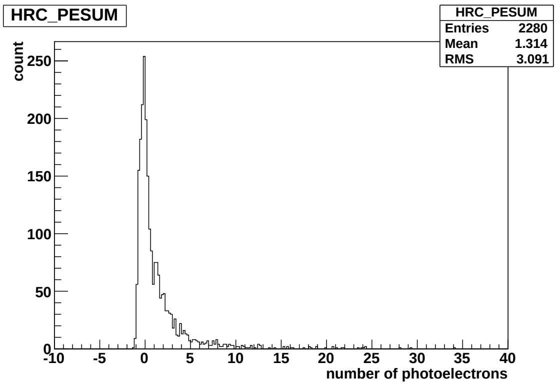

FIGURE 4.33: A histogram of the total number of p.e. for the lower velocity at an incident position (120 mm, 10 mm).

4.4 Background Rejection Capability

Relations of the rejection capability and the photoelectron threshold are shown in Figure 4.34. The rejection capability was calculated in two ways, without subtraction of multi-hit-like excess (“ + ” marker) and with its subtraction (“ × ” marker), as follows.

$$\text{(efficiency shown by “ + ”)} = 1 - \frac{\#\text{(events below the threshold)}}{\#\text{(total events)}} \tag{4.4}$$

$$\text{(efficiency shown by “ × ”)} = 1 - \frac{\#\text{(events below the threshold)}}{\#\text{(total events)} - \#\text{(multi-hit like excess)}} \tag{4.5}$$

Error bars for the “ × ” markers in Figure 4.34 are statistical errors resulting from #(events below the threshold) in Equation (4.5). For errors of very small counts, 68.27 % confidence intervals [23] were used.

In the results of both the calculations, sufficient rejection capabilities were obtained. By setting a threshold at 9 photoelectrons, rejection capability of 99.5 % can be achieved for all of the four incident positions tested. With a threshold at 7 photoelectrons, even 99.9 % rejection capability can be expected. These are quite sufficient numbers for the main experiment.

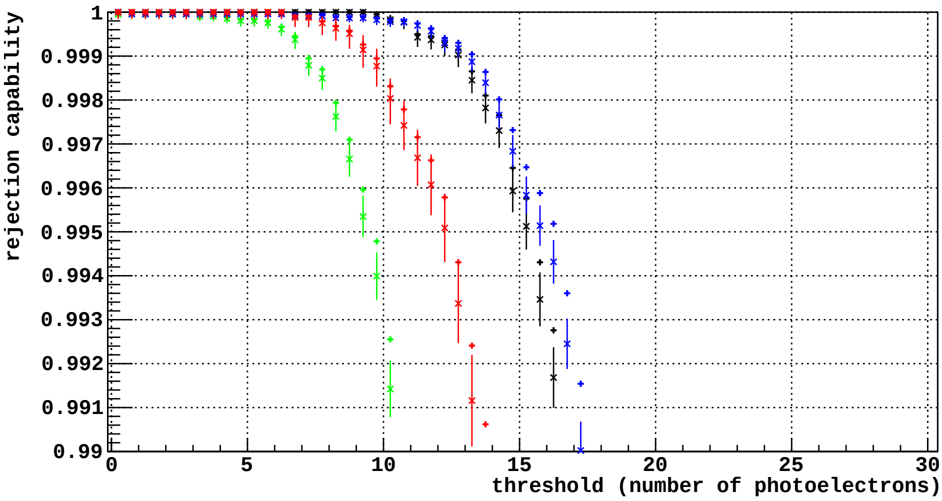

FIGURE 4.34: Relations of the rejection capability and the photoelectron threshold. The rejectioin capability was calculated in two ways: by Equation (4.4) shown by " + " marker and by Equation (4.5) shown by " × " marker. Black is at an incident position (0 mm, 0 mm), red is at (16.9 mm, 0 mm), green is at (33.8 mm, 0 mm), and blue is at (0 mm, 10 mm). Statistical errors for the " + " markers are omitted.

4.5 Signal Overkill Probability

Signal overkill probability was obtained for the twelve incident positions to HIRAC as shown in Figures 4.35 - 4.37. It was calculated as follows.

$$(\text{overkill probability}) = \frac{\#(\text{events over the threshold})}{\#(\text{total events})} \tag{4.6}$$

Statistical errors for #(events over the threshold) were taken into account. Due to the tails up to more than 10 photoelectrons seen in the histograms (Figure 4.22 - 4.33), relatively large signal overkill probabilities, for example 2 - 4 % at a nine-photoelectron threshold and 4 - 6 % at a seven-photoelectron threshold, were obtained.

In Figures 4.35 - 4.37, the overkill probability depends on the incident position. Figure 4.38 shows the tested incident positions and the overkill probabilities with the seven-photoelectron threshold. Such position-dependent overkill of signals can be a problem in the main experiment, because it may distort the final spectrum. Therefore, this signal overkill probability should be reduced or at least uniformed in position. Possible improvements for this problem are discussed in the next chapter.

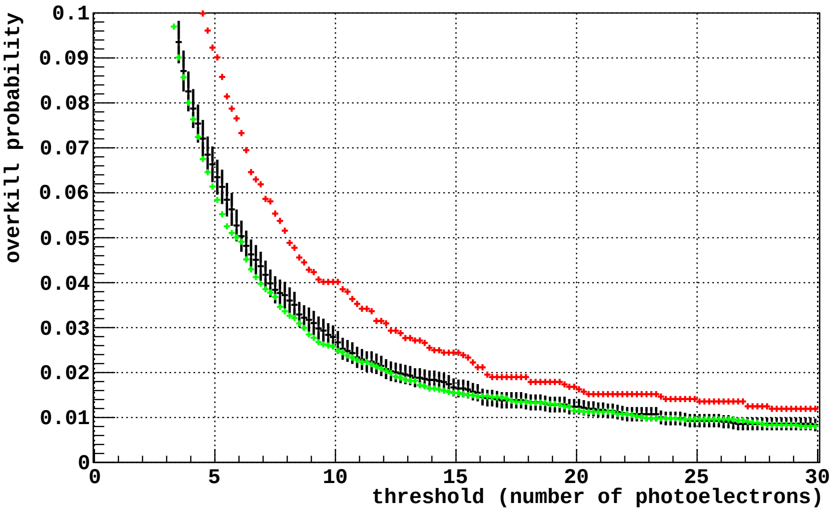

FIGURE 4.35: Overkill probabilities at incident positions near the center. Black is at an incident position (0 mm, 0 mm), red is at (0 mm, 10 mm), and green is at (16.9 mm, 0 mm). Error bars for the red and green markers are omitted.

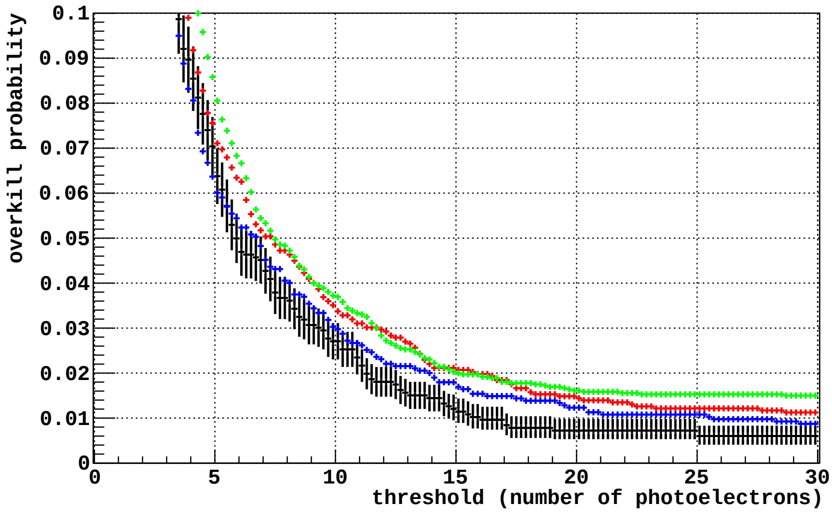

FIGURE 4.36: Overkill probabilities at incident positions x =33 − 67 mm. Black is at an incident position (33.8 mm, 0 mm), red is at (33.8 mm, 10 mm), green is at (33.8 mm, 20 mm), and blue is at (67.5 mm, 0 mm). Error bars for the red, green, and blue markers are omitted.

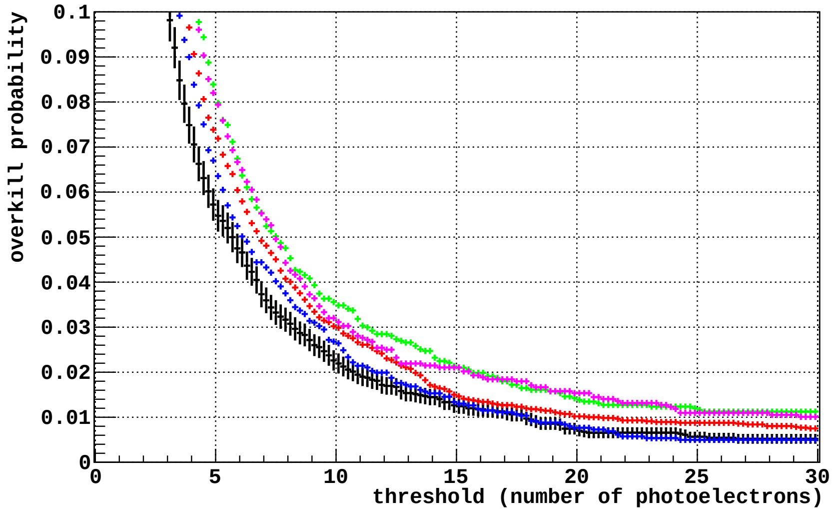

FIGURE 4.37: Overkill probabilities at incident positions near the edge. Black is at an incident position (101.3 mm, 0 mm), red is at (101.3 mm, 10 mm), green is at (101.3 mm, 20 mm), blue is at (120 mm, 0 mm), purple is at (120 mm, 10 mm). Error bars for the red, green, blue, and purple markers are omitted.

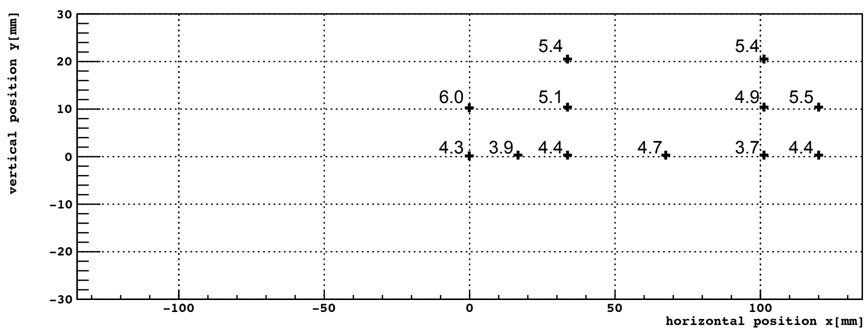

FIGURE 4.38: Tested incident positions with the lower-velocity deuterons are shown. The numbers show the obtained signal overkill probabilities in % with the seven-photoelectron threshold.

Chapter 5

Discussion

5.1 Discussion on Background Rejection Capability

In this section, the background rejection capability expected in the main experiment is discussed by taking into account the results of the test experiment.

In the test experiment, the mean values of the number of photoelectrons higher than the simulated values were observed at all the four incident positions tested with the background-like condition. The differences between them are probably because of underestimation in the simulation, described in section 2.4. In this simulation, there was underestimation mainly in two parts. The first part is the transmittance in aerogel. In the calculation, (1-(transmittance)) of photons were regarded to be killed, but some of them may be just scattered by small angles and able to reach one of the PMTs. The second part is about photons which did not reach the PMTs before entering the aerogel again. These photons were regarded as disappeared, but they may be reflected several times by the inner surface of the aerogel box and may finally reach the PMTs.

In order to take into account these two contributions, we assume that the mean values are simply corrected as the following.

$$\mu_{\text{observed}} = f\left(\mu_{\text{simulated}} + \alpha(N_{\text{max}} - \mu_{\text{simulated}})\right). \tag{5.1}$$

In this assumption, the first contribution about the transmittance is represented by a factor f, and the other contribution is represented by a survival probability α for those photons re-entering the aerogel. N_{max} was evaluated to be 32 by a calculation omitting the third line of Equation (2.5).

The parameters f and α were deduced from the plot of the mean values obtained in the test experiment and the simulated mean values shown in Figure 5.1. By fitting the four points with equal weight[1], f and α were determined to be $f = 1.3$ and $\alpha = 0.2$, respectively.

Under this assumption, the mean value of the number of photoelectrons for each incident position can be derived by applying Equation (5.1) to the result of the simulation (Figure 2.15). Then, the minimum value of the mean values in the region of interest is determined to be $\mu_{\text{min}} = 22$, and the averaged value of the mean values in the region of interest is $\mu_{\text{average}} = 26$. For these two values, the expected relations between the threshold for the number of photoelectrons and rejection capability are plotted in Figure 5.2. For this calculation, the function (4.3) was used with its parameter σ_1 obtained by the fitting. As shown in the figure, to achieve 99.5 % at any incident position in the region of interest, a threshold for the number of photoelectrons needs to be set at or less than 9 photoelectrons, and with the nine-photoelectron threshold, the rejection capability higher than 99.9 % is expected at the average position in the region of interest.

In the main experiment, with 99.5 % rejection capability, the background rate can be reduced to be about 0.25 kHz at the trigger level, and with the rejection capability higher than 99.9, it can be reduced to be even less than 0.05 kHz %. This is quite sufficient for the trigger condition in the main experiment.

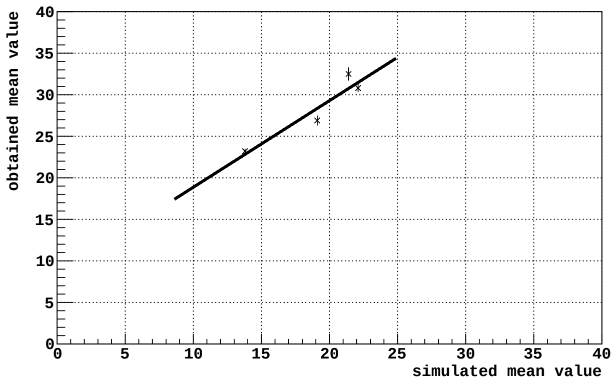

FIGURE 5.1: Comparison of the mean values obtained in the test experiment and by the simulation. The line shows the function (5.1) with $\alpha = 0.2$ and $f = 1.3$.

[1]This is because there should be larger errors in this naive assumption, though the experimental errors were evaluated.

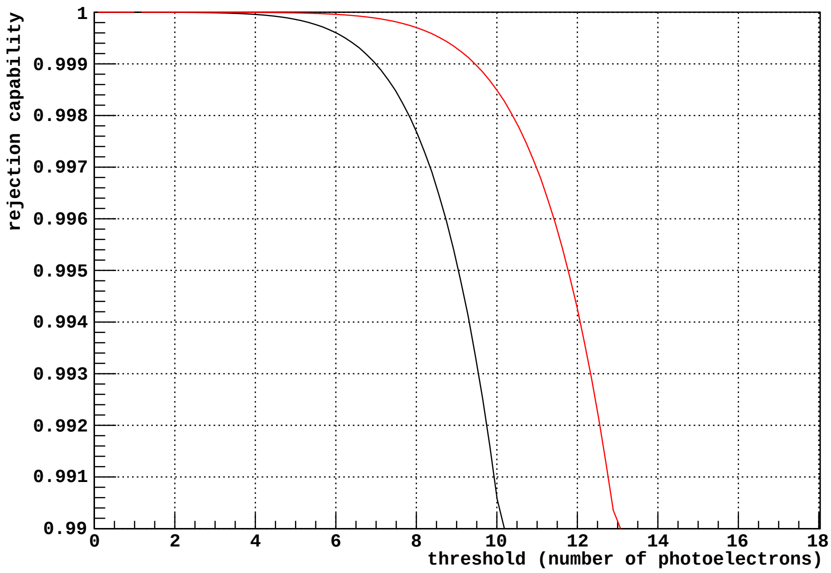

FIGURE 5.2: Expected relations between the threshold for the number of photoelectrons and rejection capability for $\mu_{\text{min}} = 22$ and 26. The black curve is for $\mu_{\text{min}} = 22$, and the red curve is for $\mu_{\text{min}} = 26$.

5.2 Discussion on Signal Overkill

In the lower-energy deuteron runs, the tails up to more than 10 photoelectrons were observed in the histograms of the total number of photoelectrons. In this section, the causes of these events are discussed.

There are two possibilities of the lower-velocity deuterons emitting Cherenkov photons. The first possibility is the Cherenkov radiation in an ultraviolet region. Since the refractive index increases in the short-wavelength region, the Cherenkov radiation in this region may occur. The other possibility is a delta ray, which is an electron scatted by the incident beam. Because the electron mass is very small compared to the deuteron mass, the velocity of the delta ray can be higher than the velocity of the incident deuterons. Then, this delta ray can emit Cherenkov photons.

First, we discuss the Cherenkov radiation in the ultraviolet region. As shown in Figure 2.4, the refractive index increases in the ultraviolet region by about 0.01. Also, there were individual differences of the refractive index about 0.01. Thus, in some of the aerogel pieces, index could reach 1.20 in the ultraviolet region. Then, the lower-energy deuterons can emit Cherenkov photons in this region of wavelength. However, this happens only in a limited wavelength region, and the total amount of Cherenkov photons are proportional to $(1 - 1/(n\beta)^2)$, which is very small in this case. Therefore, only a few photoelectrons are expected at most, and this can not account for 10 or more photoelectrons observed in the photoelectron histograms.

Next, the effect of the delta ray is evaluated. The probability of delta ray emission inside this 2 cm-aerogel was calculated, using the Mott cross section formula. The result is shown in Figure 5.3, where the upper figure is the cumulative probability of the delta rays faster than the given velocity β in the x axis of this graph, and the lower figure is the probability distribution of the delta ray emission. With a probability of 3 %, delta rays faster than $\beta = 0.93$ are emitted. These electrons can emit Cherenkov photons, but at the same time, they immediately lose their velocity. Actually their travel length with velocity faster than the Cherenkov threshold is only a few mm (e.g., 3 mm for $\beta = 0.95$ delta ray in this aerogel), and within this length, 10 or more photoelectrons are not expected. Therefore, though the delta rays can contribute the signal overkill at a few photoelectrons region, they can not explain all the tails up to more than 10 photoelectrons in the histograms.

In both the possibilities, all of the large tails could not be explained, but at least they can contribute to some part of the signal overkill. Therefore, improvements for these causes are discussed in the next section.

In addition to the above two possibilities, protons slightly accelerated by the deuteron breakup reaction were considered, but this contribution was found to be negligibly small because of the small-momentum transfer dominated by the fermi momentum. We calculated the probability of the deuteron breakup in the finger scintillators and in the lead target inside the upstream FOPI detector based on the inclusive differential cross sections of the $A(d,p)X$ reactions [24]. As a result, for example, the probability of the protons accelerated by only 0.01 in β was deduced to be about 0.06%, which is negligibly small to account for the observed signal overkill.

5.3 Improvement of Signal Overkill

In this section, we discuss possible improvements for the signal overkill and its position dependence. Because HIRAC will be installed at the dispersive focal plane, where the momentum of the signal deuterons are analyzed, position-dependent signal overkill will directly distort the final spectrum. Although this distortion might be corrected by shifting the central momentum of the spectrometer or adding a pre-scaled trigger without information from HIRAC, it is preferred to improve such signal overkill and distortion of the spectrum. In this section, we discuss three possible improvements for this problem.

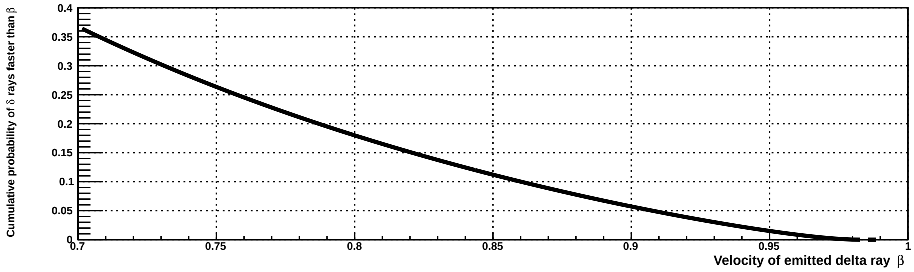

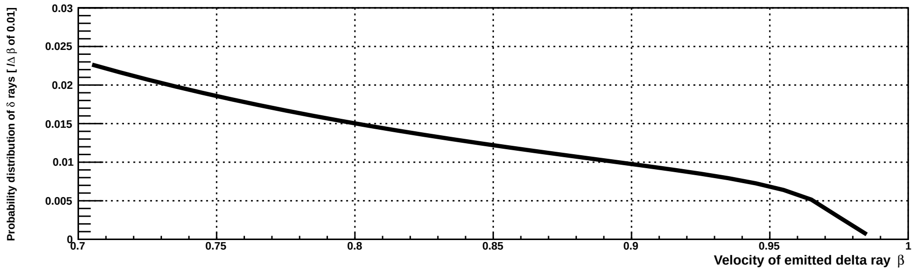

Figure 5.3: The upper figure is the cumulative probability of the delta rays faster than the velocity β. The lower figure is the probability distribution of the delta ray emission.

The first improvement is to use a lower refractive index. This will reduce the Cherenkov radiation in the ultraviolet region. To keep a refractive index below 1.18 even in the ultraviolet region, for example index of 1.16 at wavelength of 400 nm can be a candidate. With this index, the number of photoelectrons for the background protons is expected to decrease by about 14 %, which is still an acceptable number.

The second idea is to use a diffuse reflector as a reflector in back of the aerogel in HIRAC. Then, even if Cherenkov photons are emitted by delta rays or deuterons, they will diffusely reflected. This can not reduce the signal overkill, but uniform the signal overkill probability in position. Then, the distortion, which can be caused by position dependence of the signal overkill probability, will be reduced.

The third improvement is to place an additional aerogel Cherenkov detector at the middle focal plane (S2). As described in section 1.2, the momentum-compaction optics mode will be adopted from the target to S2 in order to reject secondary backgrounds. Therefore, position dependence in signal overkill probability at this position will not affect the spectrum at the final dispersive focal plane. However, a high rate including secondary backgrounds is expected at this position. Therefore, it can be used in combination with HIRAC at the final focal plane to reduce the overall position dependence of the overkill.

As near-future work, we will study on details of these improvements and prepare for the coming main experiment expected in 2013-2014.

Chapter 6

Conclusion

For the spectroscopy experiment of η' mesic nuclei, a high-refractive-index aerogel Cherenkov counter (HIRAC) has been developed. This detector has silica aerogel with a refractive index of $n = 1.18$ at wavelength of 400 nm, in order to reject background protons of velocity $\beta \sim 0.95$ at the trigger level, while signal deuterons have velocity around $\beta \sim 0.83$ in the main experiment.

A test experiment of HIRAC was performed to evaluate the background rejection capability and the signal overkill probability. The rejection capability was tested at four incident positions of HIRAC using the 1900 MeV/u ($\beta = 0.944$) deuteron beam. From the results at the four positions tested, the overall rejection capability expected in the main experiment was evaluated to be higher than 99.9% in average and 99.5% at the least-sensitive position in the entire region of interest with the nine photoelectron threshold. This is quite sufficient to reduce the background rate to the order of 0.1 kHz at the trigger level in the main experiment.

The signal overkill probability was tested at twelve incident positions with the 800 MeV/u ($\beta = 0.843$) deuteron beam. The obtained rejection capability was about 2% - 4 %, depending on the incident position, even at the nine-photoelectron threshold. It may be a problem in the main experiment, because position dependence of signal overkill may distort a final spectrum. Therefore, there is room for improvement of the detector in order to reduce the overkill and/or reduce the position dependence.

Acknowledgements

First and foremost, I would like to express my sincere gratitude to Prof. Dr. Ryugo S. Hayano, my supervisor, for his guidance in this field of physics. In the beginning of my study, fortunately I had opportunities almost every day to discuss with him on the basics of the experimental nuclear and particle physics, and there were always a lot of things I learned from his brilliant ideas.

I am deeply grateful to Dr. Kenta Itahashi and Dr. Hiroyuki Fujioka for giving me the opportunity to work on this interesting experiment. They kindly introduced me all the details of the plan of the experiment, and it was the start of my research life. Discussions with them were very interesting, and their continuous encouragements and advices were invaluable.

I would like to express my great thanks to Prof. Dr. Hans Geissel, Prof. Dr. Christoph Scheidenberger, and Dr. Helmut Weick. They kindly took care of me during my half-year stay at GSI. Discussions with them about the experiment at FRS were always very valuable. I could learn many things from their expert knowledge.

I am really grateful to Prof. Dr. Volker Metag, Dr. Mariana Nanova, Dr. Ken Suzuki, and Mr. Takahiro Nishi for their participation in the test experiment and continuous advices. Without their help, the test experiment could not be finished within the tight beam time schedule.

I am also grateful to Prof. Dr. Satoru Hirenzaki, Prof. Dr. Daisuke Jido, and Dr. Hideko Nagahiro for their theoretical contribution for the main experiment. I had many opportunities to hear their talks on η' mesic nuclei, and I could learn about theoretical aspects of the η' mesic nuclei.

I would like to express my gratitude to Dr. Makoto Tabata, who invented the new method to produce the high-refractive-index aerogel, for providing us with many pieces of them. His advices and suggestions on the aerogel were very important.

I would like to express my great appreciation to all the members of the FRS group at GSI for their kind help in the setup of the test experiment and encouragements during my stay at GSI.

I acknowledge the referees, Prof. Dr. Hayano, Prof. Dr. Hideki Hamagaki, and Prof. Dr. Kentaro Yako, for reviewing my thesis.

I wish to express my special thanks to all the members of the nuclear experiment group at the University of Tokyo for their encouragement. I could learn many things from discussion with them.

Last but not least, I would like to express gratitude to my parents for their continuous supports and encouragements.

Appendix A

Collaborators

K. Itahashi, H. Outa,
Nishina Center for Accelerator-Based Science, RIKEN, Saitama, Japan

H. Fujioka,
Division of Physics and Astronomy, Kyoto University, Kyoto, Japan

H. Geissel, H. Weick,
GSI - Helmholtzzentrum für Schwerionenforschung GmbH, Darmstadt, Germany

S. Friedrich, V. Metag, M. Nanova,
II. Physikalisches Institut, Universität Gießen, Gießen, Germany

R.S. Hayano, S. Itoh, T. Nishi, K. Okochi, T. Suzuki, Y.K. Tanaka
Department of Physics, The University of Tokyo, Tokyo, Japan

S. Hirenzaki, H. Nagahiro,
Department of Physics, Nara Women's University, Nara, Japan

D. Jido,
Yukawa Institute for Theoretical Physics, Kyoto University, Kyoto, Japan

and K. Suzuki
Stefan Meyer Institut für subatomare Physik, Vienna, Austria

Bibliography

[1] T. Hatsuda and T. Kunihiro, Phys. Rept. **247**, 221 (1994).

[2] R. S. Hayano and T. Hatsuda, Rev. Mod. Phys., **82**, 2949 (2010).

[3] K. Suzuki *et al.*, Phys. Rev. Lett. **92**, 072302 (2004).

[4] E. E. Kolomeitsev, N. Kaiser, and W.Weise, Phys. Rev. Lett. **90**, 092501 (2003).

[5] D. Jido, T. Hatsuda, and T. Kunihiro, Phys. Lett. B **670**, 109 (2008).

[6] D. Jido, H. Nagahiro, and S. Hirenzaki, Phys. Rev. C **85**, 032201(R) (2012).

[7] S. H. Lee and T. Hatsuda, Phys. Rev. D **54**, 1871 (1996).

[8] P. Costa, M. C. Ruivo, and Yu. L. Kalinovsky, Phys. Lett. B **560**, 171 (2003).

[9] H. Nagahiro and S. Hirenzaki, Phys. Rev. Lett. **94**, 232503 (2005); H. Nagahiro, M. Takizawa, and S. Hirenzaki, Phys. Rev. C **74**, 045203 (2006).

[10] H. Nagahiro, S. Hirenzaki, E. Oset, and A. Ramos, Phys. Lett. B **709**, 87 (2012).

[11] P. Moskal *et al.*, Phys. Lett. B **474**, 416 (2000).

[12] M. Nanova *et al.*, Phys. Lett. B **710**, 600 (2012).

[13] K. Itahashi *et al.*, Letter of Intent for GSI-SIS (2011).

[14] K. Itahashi *et al.*, Prog. Theor. Phys. **128**, 601 (2012).

[15] S. Barsov *et al.*, Eur. Phys. J. A **21**, 521 (2004); I. Lehmann, PhD thesis, University of Cologne (2003).

[16] H. Nagahiro *et al.*, arXiv:1211.2506 [nucl-th].

[17] M. Tabata et al. : Nucl. Instr. and Meth. A **623**, 339 (2010).

[18] K. Kleinknecht, Detectors for Particle Radiation (Cambridge University Press, Cambridge 1986).

[19] J. Beringer et al., Phys. Rev. D **86**, 010001 (2012).

[20] I. Adachi et al., Nucl. Instr. and Meth. A **639**, 222 (2011).

[21] Hamamatsu Photonics, private communication.

[22] Hamamatsu Photonics, Photomultiplier Tube R329-02, Web page, http://sales.hamamatsu.com/assets/pdf/parts_R/R329-02_TPMH1254E02.pdf.

[23] G. J. Feldman *et al.*, Phys. Rev. D **57**, 3873 (1998).

[24] V. Punjabi *et al.*, Phys. Rev. C **39**, 608 (1989).